Comparative Study On Immersion Freezing Utilizing Single Droplet Levitation Methods

Miklós Szakáll[1], Michael Debertshäuser[1], Christian Philipp Lackner[1], Amelie Mayer[1], Oliver Eppers[2], Karoline Diehl[1], Alexander Theis[1], Subir Kumar Mitra[2], and Stephan Borrmann[1,2]

[1]Institute for Atmospheric Physics, Johannes Gutenberg University, Mainz; J.-J.-Becherweg 21, D-55128 Mainz; Germany
[2]Department of Particle Chemistry, Max Planck Institute of Chemistry; Hahn-Meitner-Weg 1, D-55128 Mainz, Germany

Correspondence: Miklós Szakáll (szakall@uni-mainz.de)

Abstract. Immersion freezing experiments were performed utilizing two distinct single-droplet levitation methods. In the Mainz vertical wind tunnel (M-WT) supercooled droplets of $700\,\mu\mathrm{m}$ diameter were freely floated in a vertical air stream at constant temperatures ranging from $-5\,°\mathrm{C}$ to $-30\,°\mathrm{C}$ where heterogeneous freezing takes place. These investigations under isothermal conditions allow applying the stochastic approach to analyze and interpret the results in terms of the freezing or nucleation rate. In the Mainz acoustic levitator (M-AL) 2 mm diameter drops were levitated while their temperature was continuously cooling from $+20°\mathrm{C}$ to $-28\,°\mathrm{C}$ by adapting to the ambient temperature. Therefore, in this case the singular approach was used for analysis. From the experiments, the densities of ice nucleating active sites (INAS) were obtained as function of temperature. The direct comparison of the results from two different instruments indicates a shift of the mean freezing temperatures of the investigated drops towards lower values that was material dependent. As ice nucleating particles, seven materials were investigated, two representatives of biological species (fibrous and microcrystalline cellulose), four mineral dusts (feldspar, illite NX, montmorillonite, and kaolinite), and natural Sahara dust. Based on detailed analysis of our results we determined a material dependent parameter for calculating the freezing temperature shift due to a change in cooling rate for each investigated particle type. The analysis allowed further classifying the investigated materials to be described by a single- or a multiple-component approach. From our experiences during the present synergetic studies, we listed a number of suggestions for future experiments regarding cooling rates, determination of the drop temperature, purity of the water used to produce the drops, and characterization of the ice nucleating material. The observed freezing temperature shift is significantly important for the intercomparison of ice nucleation instruments with different cooling rates.

1 Introduction

Immersion freezing is considered to be the most effective freezing/nucleation process for ice particle production in mixed-phase clouds (Diehl and Grützun, 2018). The ice nucleation abilities of atmospheric particles have been investigated very intensively for the last decades (Hoose and Möhler, 2012). Beside in-situ measurements, laboratory-based investigation techniques are widely used to discover the basic physical and chemical processes and properties of ice nucleating particles (INP). Laboratory immersion freezing experiments aim at the characterization of the temperature dependent ice nucleation ability of different

types of INP under controlled conditions. The ice nucleation efficiency of INP is commonly expressed in terms of ice nucleation
active sites (INAS) density $n_s(T)$. This is calculated from the experimentally determined total number of nucleation events
per unit surface area of the particles. INAS density is used to represent the number of ice active sites on the particles that
are active between $0°C$ and the sub-zero temperature T (DeMott, 1995; Connolly et al., 2009; Murray et al., 2012; Hoose
and Möhler, 2012). Another important parameter employed for describing the INP nucleation ability is the nucleation rate
~~coefficent~~coefficient, i.e. the probability of nucleation at a certain temperature per unit time per unit surface area of the particle
(Vali, 2014). The nucleation rate coefficient is determined using the classical nucleation theory on experiments under isothermal
conditions (e.g., Rigg et al. (2013); Murray et al. (2011); Niedermeier et al. (2010)).

Intercomparisons of measurement techniques revealed a wide scatter of measured ice nucleation activities of particles. This
is due to differences in the measuring methods employed by the different instruments and the diversity in the sample prepara-
tion at different research sites. One essential and still not understood discrepancy arises between dry dispersion and aqueous
suspension measurement techniques (Hiranuma et al., 2019). In the former, experiments employ water vapor condensation
onto dry dispersed particles followed by droplet freezing (e.g., cloud chambers, continuous-flow diffusion chambers), while
the latter denotes experiments starting with test samples pre-suspended in water before cooling (e.g., freezing arrays, drop lev-
itators). Several studies have focused on identifying potential reasons of this data diversity. Recently, two major international
research activities were conducted and produced a large amount of new data and results, one organized around the German
INUIT (Ice Nucleation Research Unit) research community, and the FIN (Fifth International Ice Nucleation Workshop). These
intercomparison campaigns revealed data diversity over several orders of magnitude in n_s already among aqueous suspension
techniques also in case of a recommended protocol for sample treatment and preparation (Hiranuma et al., 2019; DeMott et al.,
2018). As these studies concluded, a key strategy would be to rigorously examine and define the functionality, configuration
and limitations of the measurement techniques and instruments (DeMott et al., 2018).

Widely employed measurement instruments for investigating the immersion freezing of aqueous suspensions are freezing
arrays (Murray et al., 2011; Hader et al., 2014; Budke and Koop, 2015; Schrod et al., 2016; Reicher et al., 2018; Harrison et al.,
2018). They offer the possibility of experiments at constant temperatures and determining the nucleation rate coefficient of
INP, or providing data on $n_s(T)$ when utilizing cooling rate experiments. Their advantages of inexpensive and easy operation,
and the large number of simultaneously measurable droplets offering good count statistics, promoted them for INP characteri-
zation experiments. In our study we take a step further to real atmospheric conditions of cloud droplets, and avoid the contact
of any supporting surface. The single droplet levitation techniques employed offer experiments with natural droplet shapes
and contact-free levitation, where the heat conduction of the released latent heat during freezing also better meets atmospheric
conditions. The main disadvantage of the single droplet levitation techniques is the limited number of individual droplet mea-
surements they provide. In order to get statistically relevant numbers of data points, a series of experiments has to be conducted
by an operator over a long time period, and, therefore, the long-term variation of the environmental conditions might lead to
measurement uncertainties. Prominent single droplet levitation techniques used for immersion freezing are an electrodynamic
balance (Rzesanke et al., 2012; Hiranuma et al., 2015) in which a charged supercooled droplet of about $100\,\mu m$ is levitated
between electrodes; an acoustic levitator (Ettner et al., 2004; Diehl et al., 2014), and a vertical wind tunnel (von Blohn et al.,

2005; Diehl et al., 2011, 2014). An optical levitator for freezing experiments was also reported (Ishizaka et al., 2011), however,
to our best knowledge it has not yet been applied for investigating immersion freezing.

In the Mainz vertical wind tunnel laboratory at the Johannes Gutenberg University of Mainz, Germany, we have conducted immersion freezing experiments with aqueous suspensions employing two independent single droplet levitation techniques within the framework of the Research Unit INUIT. Our laboratory hosts two major facilities, both attaining contact-free levitation of liquid droplets and cooling of the surrounding air down to about $-28°$C. The main equipment is the Mainz vertical wind tunnel (M-WT) where atmospheric hydrometeors are investigated in an air updraft maintained by means of two vacuum pumps (Szakáll et al., 2010; Diehl et al., 2011). All hydrometeors are floated at their terminal falling velocities so that the relevant physical quantities, as for instance the Reynolds number and the ventilation coefficient (i.e. the ratio of the water vapour mass flux from the drop for the cases of a moving and a motionless drop), are equal to those in the real atmosphere. The experiments in M-WT are carried out at constant temperatures. The instrumentation of the laboratory is complemented by a walk-in cold room in which the Mainz acoustic levitator (M-AL) is situated. In M-AL the free levitation is achieved at the nodes of a standing acoustic wave (Ettner et al., 2004; Diehl et al., 2014). Although M-AL does not simulate atmospheric air flow conditions as M-WT, its simple setup, and the possibility of the direct measurement of drops' surface temperature promoted it for immersion freezing measurements utilizing cooling rate experiments (DeMott et al., 2018).

The goal of the present study was to conduct a synergetic investigation of the immersion freezing ability of various INP using two qualitatively different free levitation methods. Furthermore, we aimed to provide direct intercomparisons of laboratory instruments implementing different cooling rate conditions in immersion freezing experiments. Therefore, we carried out immersion freezing experiments in M-AL and M-WT by using aqueous samples of INP of different origin and types (biological particles as well as proxy and natural mineral dusts). The theoretical background of the drop and INP characteristics in drop levitating techniques is summarized in Section 2. The experimental setups for the synergetic study employing M-WT and M-AL are introduced in Section 3. We present and discuss our experimental results in Section 4 and conclude with a summary and an outlook for future experiments in Section 5.

2 Theoretical background of heterogeneous freezing

The heterogeneous nucleation of ice, i.e. the phase transition from liquid to solid state of water induced by the growth of ice embryos on nucleation sites on INP, takes place at different temperatures, depending on the properties of the particles immersed in water (Vali, 2014). The larger the particle, the higher is the possibility that some part of its surface favours ice nucleation. Hence, the probability of freezing (or ice nucleation) is dependent on the total surface area of the particles (Hoose and Möhler, 2012). Nevertheless, freezing is a dynamic process in which molecules from the metastable liquid state are joining to (and detaching from) the growing ice embryo. Therefore, nucleation is a time-dependent process and occurs under isothermal conditions as well (i.e. when the temperature remains constant). The interpretations of experimental immersion freeezing results in the literature are based either on the stochastic (time and temperature-dependent) or on the singular (temperature-dependent) hypothesis, depending on the experimental conditions. The stochastic approach is based on classical nucleation

theory and represents a physical description, therefore, it can be applied even outside the experimentally investigated range of timescales and surface areas. In contrast, the assumptions underlying the singular approach are not consistent with experimental observations, thus, it is not a physical but an empirical description and its application is restricted to the conditions during the measurements.

2.1 Stochastic approach

In experiments under isothermal conditions the number of unfrozen supercooled aqueous suspension droplets in a population decays exponentially with time, because at any point in time the number of freezing droplets is a function of the (decreasing) number of still unfrozen droplets. The underlying assumption here is that each droplet freezes with the same probability when they contain identical INP. The rate R_n which is used to describe this decay at a fixed temperature is determined from the number of the observed freezing events per unit time as (see Vali (2014) for detailed discussion)

$$R_n(t,T) = -\frac{1}{N_{tot} - n_{fr}} \frac{dn_{fr}}{dt} \tag{1}$$

where n_{fr} denotes the number of frozen droplets at time t, and N_{tot} the total number of droplets in the population, i.e. the total number of the investigated individual droplets. After integrating Eq. (1) and assuming constant, i.e. time independent freezing rate at a fixed temperature, the well-known expression follows:

$$R(T) = -\frac{\ln\left(1 - \frac{n_{fr}}{N_{tot}}\right)}{t} \tag{2}$$

In the stochastic approach, the time dependence of nucleation is taken into account by introducing the heterogeneous nucleation rate coefficient J_s – similarly to that for homogeneous nucleation (Pruppacher and Klett, 2010) –, which gives the rate of change of the number of ice embryos per unit surface area of the ice nucleating particle. (In case of homogeneous nucleation J_{hom} is given per unit volume of liquid drop.) If all droplets in the population contain the same amount of particle surface, each ice nucleating sites of the particles are equivalent, and any part of the particle surface has an equal likelihood of containing an ice nucleating site, the system is named single-component (Broadley et al., 2012; Herbert et al., 2014). Then, by definition,

$$J_s(T) = \frac{R(T)}{S_p} \tag{3}$$

Here S_p is the total particle surface area in each aqueous suspension droplet which can be calculated as

$$S_p = V_d \cdot c \cdot SSA \tag{4}$$

with V_d being the drop volume, c the particle mass concentration in the sample solution, and SSA the specific surface area of the particle. In case of any interparticle variability in the ice nucleating ability of the particle population Eq. (3) cannot be used. Such a system is called multiple-component (Vali et al., 2015), which, however, can be divided in subpopulations of equally ice active entities. Each subpopulation i can be treated as single-component and characterized by its number density $n_{s,i}$ and nucleation rate coefficient $J_{s,i}$ (Murray et al., 2011).

2.2 Singular approach

The concept of the singular approach is based on the observation that freezing of drops containing INP occurs at a characteristic temperature once they are subjected to cooling. This also implies that supercooled droplets remain unfrozen arbitrarily long when exposed to a temperature T, even if they contain INPs which trigger freezing only at an INP-specific $T_c < T$. Hence, the time dependence of ice nucleation is assumed to be of secondary importance in comparison to the particle to particle variability of the ice-nucleating ability (Connolly et al., 2009). In this concept ice nucleation occurs on particular sites on the surface of a particle, the so-called ice-nucleating active sites (INAS), as soon as a temperature is reached which is characteristic for the INP material and its nucleating properties. Reaching this temperature by cooling, the droplet including the INP freezes instantaneously. For the singular approach, the INAS surface density $n_S(T)$ is defined as the cumulative number of sites per surface area that become active between $0°C$ and T, and can be expressed as

$$n_s(T) = -\frac{\ln(1 - f_{ice}(T))}{A} \tag{5}$$

where $f_{ice}(T) = \dfrac{n_{fr}(T)}{N_{tot}}$ is the frozen fraction, i.e. the cumulative fraction of droplets frozen between $0°C$ and T in the population.

If all droplets were of same size and contained identical INP with homogeneous surfaces and uniform ice-nucleating sites, then f_{ice} would be a unit step function at a characteristic temperature. Variability of INP in experiments arising from diverse compositions, particle sizes, and locations of INAS on particles' surface results in a distribution of characteristic temperatures, i.e. freezing probabilities of aqueous suspension droplets, which is represented by $f_{ice}(T)$.

2.3 Cooling rate experiments

In practice, f_{ice} can be determined when a population of aqueous suspension droplets is continuously or stepwise cooled down, and the number of freezing events as the function of time or temperature is registered. Cooling rates in, e.g., freezing array (or cold stage) experiments range from 1 to $10\,\mathrm{K\,min^{-1}}$, representing also typical atmospheric rates. Employing a constant cooling rate r in the experiments, the temperature decreases with $\delta T = r\delta t$ within a time interval δt. The number of frozen droplets per unit temperature interval in a single-component system is then calculated using the stochastic approach by rearranging Eq. (2) and Eq. (3) to (e.g., (Vali and Stansbury, 1966)):

$$\frac{1}{N_{tot} - n_{fr}} dn_{fr} = -\frac{A \cdot J_s(T)}{r} dT \tag{6}$$

This equation indicates that the number of frozen droplets at a given supercooling T decreases with an increasing cooling rate. Observations revealed that the nucleation rate coefficient is an exponential function of the temperature (Vali, 2014; Broadley et al., 2012; Murray et al., 2011; Broadley et al., 2012; Wright and Petters, 2013; Herbert et al., 2014):

$$\ln J_s(T) = -\lambda \cdot T + \phi \tag{7}$$

The gradient of the logarithm of the nucleation rate coefficient, λ, is a material-dependent parameter, while ϕ is the relative nucleating efficiency of the INP. The conventional unit of λ is $\mathrm{K^{-1}}$ reflecting its empirical definition by neglecting the units of

$\ln J_s$. Integration of Eq. (6) then yields to (Vali and Stansbury, 1966)

$$-\ln\left(\frac{1 - n_{fr}}{N_{tot}}\right) = \frac{A}{\lambda \cdot r}\exp\left(-\lambda \cdot T + \phi\right) \tag{8}$$

This equation shows that the same number of frozen droplets of a population occurs at different temperatures when using
different cooling rates. The temperature difference calculated from Eq. (8) for cooling rates r_1, and r_2 is

$$\Delta T_f(r_1, r_2) = \frac{1}{\lambda}\ln\left(\frac{r_1}{r_2}\right) \tag{9}$$

The shift of the mean freezing temperatures ΔT_f was analyzed by Vali (2014) for a set of experimental data from the literature.
For discussing the data, the temperature derivative of the logarithm of the experimentally determined freezing rate normalized
by the aerosol total surface area was utilized:

$$\omega = -\frac{d\ln(R/A)}{dT} \tag{10}$$

Following from this empirical definition, the unit of ω is K^{-1} similarly to λ (cf. Eq. (7)). When $\lambda^{-1} = \omega^{-1}$, then the single-
component stochastic approach leading to Eq. (9) holds and can be applied for calculating the temperature shift caused by
different cooling rates. It was found, that for kalonite and vulcanic ash samples shown in Herbert et al. (2014) this approach
was applicable. For the majority of the revised data Vali found $\lambda^{-1} > \omega^{-1}$, thus, the observed temperature shifts were smaller
than predicted by the stochastic model. This deviation might be the results of ice nucleating sites of different effectiveness
in INP samples. Herbert et al. (2014) showed that applying a multiple-component stochastic model can indeed describe this
behavior. For single-component systems Eq. (3) can be applied (i.e. $R/A = J_s$), and therefore, the approach of Herbert et al.
(2014) resulted in $\omega = \lambda$, while for a multiple-component system $\omega \neq \lambda$. In this approach, λ is calcuated from the temperature
adjustment which brings two data sets into agreement. The two data sets in Herbert et al. (2014) were $n_s(T)$ spectra determined
either by isothermal experiments utilizing two different residence times, or by cold stage experiments using two different
cooling rates. For the former case Herbert et al. (2014) used a temperature shift analogue to Eq. (9):

$$\Delta T_{iso}(t_1, t_2) = \frac{1}{\lambda}\ln\left(\frac{\lambda \cdot t_1}{t_2}\right) \tag{11}$$

where t_1 and t_2 are the the period of time for which the particles are exposed to a constant temperature. For the cooling
rate experiments $n_s(T)$ was determined by applying the singular approach. Although the singular approach excludes any
temperature shift due to a change in cooling rate, there are experimental evidences contradicting this prediction (e.g., Vali
(1994)). Such observations resulted in the so-called modified singular description (Vali, 1994; Murray et al., 2011) which
offsets the $n_s(T)$ spectrum to lower temperatures when higher cooling rates are applied. In accordance with this empirical
description Herbert et al. (2014) shifted the $n_s(T)$ spectra to

$$n_s(T) \rightarrow n_s\left(T - \frac{\ln\left(|r|\right)}{-\lambda}\right) \tag{12}$$

From their analysis Herbert et al. (2014) revealed that kaolinite and vulcanic ash samples can be described by the single-
component stochastic approach, whereas for K-feldspar and mineral dust a multiple-component approach has to be applied.

For comparative analysis of the ice nucleating ability of particles investigated by different experimental approaches, λ is a crucial parameter. Large values of λ indicate effective INP and, therefore, weak time dependence, while less effective INP possess small λ values. Herbert et al. (2014) determined λ for a set of ice nucleating materials and compared to several literature data. The large variability of λ on the material of the INP necessitates further quantification of λ for other atmospherically relevant INP species. The lack of laboratory data of λ and ω in the literature was also highlighted by Vali (2014).

In this study we measured the frozen fraction $f_{ice}(T)$ of seven INP materials with two different methods, one utilizing isothermal conditions (M-WT), while in the other the temperature decreased continuously (M-AL). From the isothermal M-WT experiments the freezing rate and its gradient ω was determined. Furthermore, from the measured $f_{ice}(T)$ we calculated the INAS density n_s using Eq. (5). From the non-isothermal M-AL measurements $n_s(T)$ was obtained by applying the singular description. Following the approach of Herbert et al. (2014), the temperature adjustment was determined which brings the two n_s spectra into agreement. In this way the material dependent parameter λ was calculated. We analysed the λ and ω values of different INP material, and tested whether a single- or a multiple-component description can be applied to model their ice nucleation behaviour. For the temperature shifts we normalized the cooling rate in Eq. (9) using a standard value of $1\,\mathrm{K\,min^{-1}}$, which results in

$$\Delta T_f = \frac{1}{\lambda} \ln\left(\frac{1}{|r_{exp}|}\right) \tag{13}$$

In isothermal experiments the temperature shift was normalized by applying a standard time of $60\,\mathrm{s}$ (corresponding to a cooling rate of $1\mathrm{K\,min^{-1}}$) as

$$\Delta T_{iso} = \frac{1}{\lambda} \ln\left(\frac{\lambda \cdot t_{res}}{60\,\mathrm{s}}\right) \tag{14}$$

where t_{res} is the characteristic residence time of droplets in the experiments.

The isothermal M-WT and cooling rate M-AL measurements were related to each other in terms of frozen fraction. setting the total observation time in M-WT in terms of the frozen fraction. The total observation time in the M-WT experiment was calculated to reach the same f_{ice} as a cooling rate experiment using the equation given by Herbert et al. (2014):

$$t_{iso} = \frac{1}{\lambda \cdot r} \tag{15}$$

Applying the standard cooling rate of $1\mathrm{K\,min^{-1}}$, and a typical λ value of 2, a total observation time of 2 30 seconds is obtained.

2.4 Surface temperature of freely levitating droplets in freezing experiments

As becomes obvious from the description above, the correct representation of the drop temperature in freezing experiments is of crucial importance. In freezing array experiments the droplet temperatures are assumed to be equal to the substrate temperature which is directly measured by a thermometer. Since the contact area between a droplet and the substrate is large, this is an appropriate assumption even for relatively large drops with volumes of microliters. In single levitating techniques, as in M-WT or M-AL, the droplets are subjected to continuous cooling by heat diffusion and convection. The surrounding medium is air, which is a far worse heat conductor than the substrates used in freezing array experiments. The effect of this adaptive droplet
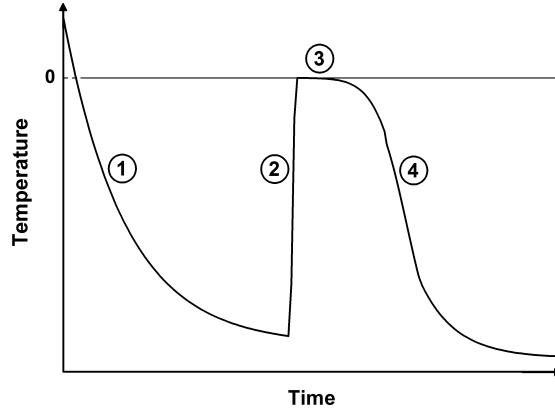
Figure 1. Schematic plot of the temporal surface temperature evolution of a freezing droplet. 1) Supercooling of the liquid droplet until nucleation is initiated; 2) Adiabatic freezing stage where rapid kinetic crystal growth takes place until supercooling is exhausted. No heat exchange with the environment; 3) Diabatic freezing stage in which ice crystal growth inside the droplet is governed by heat transfer with the environmental air; and 4) Cooling stage where the ice particle cools down adapting to the ambient temperature.

cooling becomes significant for drops with volumes in the microliter range (equivalent to sizes in the millimeter range), because the amount of latent heat to be dissipated increases with volume as does the surface area of the drops.

215   The freezing process of a single aqueous solution droplet is depicted in Fig. 1 following the concept of Hindmarsh et al. (2003). After injection, the relatively warm droplet cools down (stage 1 in Fig. 1), and its surface temperature T_a approaches an equilibrium temperature T_e determined by the ambient temperature T_∞, the dew point, and ventilation (Pruppacher and Klett (2010); and Appendix):

$$T_a(t \to \infty) = T_e \qquad (16)$$

220 In case of an evaporating droplet the equilibrium surface temperature is always lower than the ambient temperature due to evaporative cooling. For a droplet in a continuous air flow, the temperature difference between the drop and its environment is further enhanced by ventilation, resulting in a net temperature deviation δ (s. Appendix):

$$T_\infty - T_e = \delta \qquad (17)$$

The temporal evolution of the surface temperature for a droplet placed in a cold environment is described mathematically by 225 an exponential decay function (s. Appendix for the derivation):

$$T_e - T_a(t) = T_\infty - T_a(t) - \delta = [T_\infty - T_a(t=0) - \delta] \exp(-t/\tau) \qquad (18)$$

with τ being the relaxation time, i.e. the time constant of the temperature adaptation. The main physical parameters that determine τ, and therefore, the total cooling time of the droplet, are the drop size, the ventilation coefficient, as well as the

ambient temperature and dew point (s. Appendix B2). Hence, for given experimental conditions, the temporal evolution of the drop's surface temperature in stage 1 can be calculated using Eq. 18. In cold stage experiments freezing stage 1 proceeds very quickly due to the large contact area (Harrison et al., 2018); in single levitation techniques this can take up to several minutes. Drop freezing occurs at some instant in time or at some specific temperature. As soon as nucleation is initiated inside the supercooled drop, rapid kinetic crystal growth takes place (stage 2 in Fig. 1). This process is characterized by a sudden temperature increase due to the release of latent heat (which predominantly diffuses into the droplet) until the supercooling is exhausted and the drop surface temperature rises to the ice-water equilibrium temperature (i.e. to $0\,^{\circ}\mathrm{C}$ when the water activity of the investigated sample is ≈ 1, as it was in our experiments). For the drop freezing experiments this characteristic temperature or time instant is to be measured, see Section 3.2. Subsequently, a diabatic freezing of the whole droplet takes place (stage 3). The temporal duration of this freezing stage is determined by the heat exchange between the particle and its environment, therefore it proceeds slower than stage 2. In the end, the frozen particle cools down to the ambient temperature (stage 4).

3   Methods

3.1   Material and sample preparation

The experiments were carried out using seven different types of materials which are listed in Table 1. All of these materials are considered to be important constituents of atmospheric ice nucleation particles. As biological INP surrogates we investigated two cellulose types, microcrystalline and fibrous cellulose (hereafter MCC and FC, respectively). Among the investigated mineral dust materials feldspar (especially K-feldspar) exhibits the highest ability to initiate ice formation. It is a prevalent component of desert dusts so that by scaling down it is representative for dust samples in dependence on their composition (Atkinson et al., 2013). Illite NX can be considered as proxy for desert dust since their mineralogical compositions are similar (Broadley et al., 2012). Montmorillonite K10 and kaolinite (SigmaAldrich) are commercially available and characterized mineral dust materials of relevance for the atmosphere, which also have been subject of several previous studies. Furthermore, we used a natural desert dust particle sample, the ice nucleation abilities of which have been investigated with different measurement techniques during the INUIT09 measurement campaign (Ullrich et al., 2019).

Atmospherically relevant INP exhibit an extremely wide range in their ability to heterogeneous freezing. Furthermore, there is a large spread in the specific surface area (SSA) of the investigated materials from around $1\,\mathrm{m^2\,g^{-1}}$ to $245\,\mathrm{m^2\,g^{-1}}$ (s. Table 1). We chose therefore diverse mass concentrations for each of the different particle types to obtain reasonable numbers of freezing events within the temperature ranges of our measurement facilities. Furthermore, since the volume of the investigated droplets in M-AL was approximately 20 times larger than in M-WT, we used reduced mass concentrations in M-WT to obtain overlapping freezing curves with the two methods (s. Eq. (5)).

Prior to each set of experiments, 20 to 40 mL aqueous suspension was prepared by mixing sample particles of known weight (measured by an analytical balance from Sartorius) with high purity water (CHROMASOLV water for HPLC, Sigma-Aldrich). Between the measurement runs the aqueous suspension was continuously stirred at a very low rate using a magnetic stirrer to

Table 1. Aerosol material and sources measured in the current study. Also given are the specific surface area (SSA) and the concentrations used for the immersion freezing experiments in M-AL and in M-WT.

Sample material	SSA $(m^2\,g^{-1})$	Concentration $(g\,L^{-1})$
Fibrous cellulose[a] (FC; Sigma, C6288)	1.31 ± 0.1	1.0
Microcristalline cellulose[a] (MCC; Aldrich, 435236)	1.44 ± 0.1	1.0
Feldspar[b] (Microcline) (IAG TU Darmstadt)	1.79	0.5 / 0.66 / 0.8
Illite NX [c] (Arginotec)	124.4 ± 1.5	0.25/2.5
Kaolinite (Sigma Aldrich)	8.33	0.1/1.0/1.265
Montmorrillonite K10 [d] (Sigma-Aldrich)	245 ± 20	5.0
SDB01[0] (Bodele-Depression, Ts)	26	1.0 / 0.1

[a] Same as used in Hiranuma et al. (2018)
[b] Same as FS01 in Peckhaus et al. (2016)
[c] Same as in Diehl et al. (2014) and Hiranuma et al. (2015)
[d] Same as in Diehl et al. (2014)
[d] Same as in Ullrich et al., (2019)

avoid coagulation and sedimentation of the particles in the suspension. A hypodermic syringe was used to inject suspension droplets into the measuring instruments. For the M-AL measurements, the syringe was filled with aqueous suspension after an idle time of about 30 minutes without stirring (following the sample preparation protocol of Hiranuma et al. (2019)), so that
265   at the uppermost part of the solution a homogeneous suspension was generated. For the M-WT measurements we abandoned an idle time, because in this case we could presume already homogeneous suspension due to the low particle concentration. Furthermore, the syringe was shaken prior to droplet injection both in M-AL and M-WT experiments to homogenize the particle distribution in droplets. Otherwise no pre-treatment procedures were applied.

     Although efforts were made to unify and standardize the sample generation, we cannot rule out INP surface area variation
270   among the investigated droplets. There are several sources of uncertainty in total surface area inside droplets like: inhomogeneous distribution of particles among injected droplets, externally or internally mixed particles, aggregation due to sedimentation and internal circulation. The most appropriate way to determine the actual INP surface area would be the continuous

Table 2. Characteristics of the experiments conducted with M-WT and M-AL.

Characteristics	M-WT	M-AL
Thermal condition	isothermal	continuous cooling
Droplet cooling time	4 to 6 s	10 to 120 s
Freezing approach	stochastic or singular	singular
Deliverables	n_s, R/A	n_s
Temperature range	-10 to $-30°$C	-15 to $-25°$C
Droplet diameter	$700\,\mu$m	$2\,$mm
volume	$0.18\,\mu$L	$4\,\mu$L

measurement of the surface area inside each droplet under investigation, but that seems not feasible currently. Another possibility is the measurement using size-selected particles, as in the study of Hartmann et al. (2016). ~~The~~ Neglecting the variability of composition and surface area of INP may introduce significant error in calculated $n_s(T)$ and $J_s(T)$ (Barahona, 2020). Furthermore, ~~t~~he assumption of identical INP surface area in each droplet imposes a cooling rate and surface area dependence on $J_s(T)$ ~~(Alpert and Knopf, 2016)~~ (Alpert and Knopf, 2016; Knopf et al., 2020). In our analysis we considered the error sources in concentration determination, in SSA, and in droplet size for determining the propagated error for the calculated parameters.

3.2 Experimental setups and procedures

The characteristics and deliverables of the M-WT and M-AL instruments essential for the present study are summarized in Table 2 and will be described in the following subsections. Detailed descriptions of the experimental facilities are given, e.g., in Szakáll et al. (2010); Diehl et al. (2011, 2014).

3.2.1 M-WT (Mainz vertical Wind Tunnel)

The Mainz vertical wind tunnel (M-WT) is a world-wide unique experimental facility designated for the laboratory investigation of atmospheric hydrometeors, such as cloud droplets, raindrops, graupel, hailstones, and snowflakes. Single hydrometeors are floated freely at their terminal velocities in the laminar vertical updraft of the wind tunnel. Hence, the relevant physical properties of the hydrometeors, such as Reynolds numbers and ventilation coefficients, are equal to their values in the real atmosphere (Szakáll et al., 2010; Diehl et al., 2011).

For the immersion freezing experiments the air in the M-WT was cooled down and kept constant (within $\pm0.3°$C) at various temperatures between -15 and $-30°$C. For appropriate measurement statistics, at each temperature, particle type, and INP concentration, a total number of 70 aqueous suspension droplets were investigated. After injection, each droplet was floated in the M-WT until it froze, or until the experiment was terminated because of reaching a predefined time limit. The onset of
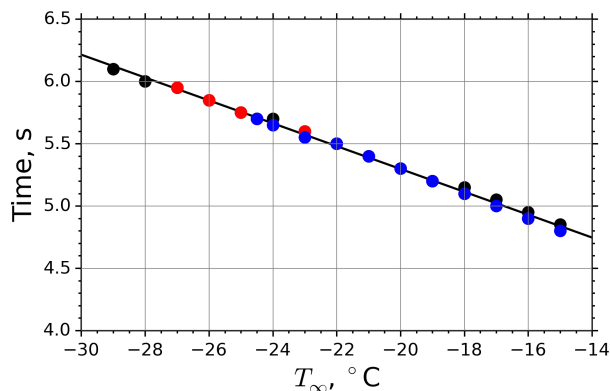
Figure 2. Time needed to approach the equilibrium temperature T_e with an accuracy of $0.2\,°C$ as the function of air temperature T_∞. Calculations carried out for dew point temperatures -30, -27.5, and $-25°C$ are plotted by black, red, and blue dots, respectively. The data points were calculated using Eq. (B21). The regression line is $t_a = 3.46 - 0.09T_\infty$ (T_∞ in $°C$).

freezing is characterized as a sudden significant change in floating behavior of the droplet caused by the irregular shape of the frozen particle. This changing behavior was visually observed and registered by the operator during the experiments. In this way, the total observation time, i.e. the time duration from injection until the onset of freezing was recorded (Diehl et al., 2014). When a droplet did not freeze within 35 seconds, it was counted as unfrozen. In our earlier immersion freezing studies we levitated the supercooled droplets for at most 30 seconds (if freezing was not initiated sooner), in accord with Eq. (15). We extended this total observation time by 5 seconds to consider the approximate time period a drop needed to approach its equilibrium temperature in M-WT (Fig. 2). Furthermore, wind speed, air temperature, and dew point temperature (typically in a range from -20 to $-35\,°C$) in the wind tunnel were recorded continuously at $2\,Hz$ temporal resolution.

The drop surface temperature was calculated using Eq. (B21) considering thermal steady state condition between the levitating drop and its surrounding air. The time needed to approach the equilibrium temperature in the M-WT experiments within $0.2\,K$ difference (i.e. below the temperature measurement precision of the applied PT100 sensor) was calculated at distinct M-WT air temperatures and plotted in Fig. 2 for different dew points. In the calculations the starting drop temperature was set to $20\,°C$. One can observe a slight dependence of the adaptation time on the air temperature, but T_e was typically reached within 5 to 6 seconds for air temperatures between -15 and $-28\,°C$. In the calculations, dew points of -30, -27.5, and $-25\,°C$ were applied and the results are merged in the plot shown in Fig. 2. Hence, the adaptation time was found to be practically independent on the dew point for the M-WT experiments.

Typical droplet diameters/volumes were approximately $700\,\mu m/0.18\,\mu L$. The size of each investigated droplet was determined from its terminal velocity (Beard, 1976), i.e. from the vertical air speed needed for freely suspending it, which can be measured with high accuracy in the M-WT (Diehl et al., 2014).

Immersion freezing in M-WT experiments was investigated under isothermal measurement conditions, hence, the stochastic approach was applied for data analysis. Since the M-WT experiments represent isothermal measurement conditions, the stochastic approach was applied first for data analysis. Thus, the rate constant R and the nucleation rate coefficient J_{het} were

315 calculated from Eqs. 2 and 3, respectively, using the number of freezing events as function of the freezing time. In the analysis the freezing time of each droplet was calculated by subtracting the adaptation time (Fig. 2) from the total observation time lasting from droplet injection until the onset of freezing. Furthermore, from the number of freezing events over the whole observation time period the frozen fraction $f_{ice}(T)$ and the INAS density $n_s(T)$ (Eq. 5) were determined employing the singular approach by equating $R \cdot t$ to n_s.

320 Background measurements were carried out before each experimental run by floating at least 10 HPLC (high purity liquid chromatography) water droplets for 35 seconds in the tunnel. We have not observed any freezing event during these test measurements, which indicates the absence of impurities (i.e. background active INP) both in the HPLC water droplets and in the wind tunnel.

3.2.2 M-AL (Mainz Acoustic Levitator)

325 The main component of the M-AL measurement facility is an acoustic levitator (APOS BA 10, tec5 GmbH), in which contact-free single droplet levitation is maintained by a standing ultrasonic wave (Diehl et al., 2014). The M-AL is placed inside a walk-in cold room where the ambient temperature was set to be $-30\,^{\circ}\mathrm{C}$ for the freezing experiments. In order to prevent any disturbing air motion, which might cause unsteady temperature condition and unstable levitation, or carry ice nucleating particles onto the levitating drop surface, the M-AL was surrounded by a protective acrylic housing. Using this setup, the air

330 temperature in the M-AL was $-28\,^{\circ}\mathrm{C}$ as measured by a PT100 sensor. An infrared thermometer (KT 19.82 II, Heitronics) and a digital video camera (USB-CAM-103H, Phytek GmbH) were arranged around the acrylic housing of the levitator.

One of the main advantages of the experimental setup of M-AL is the direct observation of the surface temperature of the levitated drops during the cooling-freezing process, which was performed by the infrared thermometer at a rate of $2\,\mathrm{Hz}$. The minimum observable spot size of the infrared thermometer restricted the minimum levitated drop diameter to $2\,\mathrm{mm}$. The actual

335 drop size was determined from the images captured by the digital video camera instantaneously after injecting the drop into M-AL. An example of a video recorded during an experiment on the ice nucleation ability of cellulose is provided as video supplement of this paper (see https://doi.org/10.5446/46729). In the video the air temperature in the cold room measured by a PT-100 sensor, the continuously determined drop size (as the volume equivalent diameter), and the drop surface temperature measured by the infrared thermometer are displayed. The recorded drop cools continuously adapting its temperature to the

340 ambient temperature until the freezing is initiated at about $-21.8\,^{\circ}\mathrm{C}$. The onset of freezing can be observed by the sudden change in the transparency of the droplet and the increase of the drop surface temperature to $0\,^{\circ}\mathrm{C}$.

In case of M-AL experiments, the droplet surface temperature approached to the equilibrium temperature in a slower manner as in M-WT, which was primarily due to the larger drop size and smaller ventilation effect stemming from the acoustic field (s. Appendix B3). The relatively moderate cooling and large drop surface area enabled us to determine the freezing temperature

345 of the individual drops with high accuracy by the infrared thermometer. In Fig. 3 two typical examples of M-AL measurements
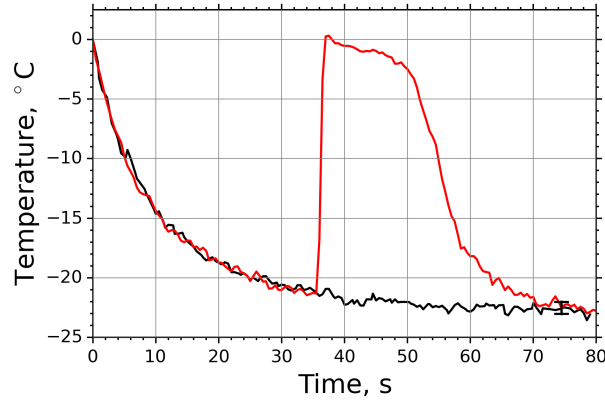
Figure 3. Measured surface temperatures of two droplets levitated in M-AL: examples of freezing (red line) and non-freezing (black line) events. The measurement uncertainty of the temperature was $\pm 0.5\,\mathrm{K}$.

are plotted: In one case (black line) no freezing occurred and the experiment was terminated after 80 seconds measurement time. In the other case (red line), freezing was initiated after 35.5 seconds cooling at about $-21.3\,^{\circ}\mathrm{C}$ surface temperature. The arithmetic mean of the three recorded temperatures preceding the deepest drop surface temperature during the last 1.5 seconds before the onset of freezing, i.e. the temperature at transition from stage 1 to stage 2 in Fig. 1, was considered as the freezing temperature. The number of frozen droplets was measured and binned in $1\,\mathrm{K}$ intervals to calculate f_{ice}, and thereof n_s applying the singular approach (Eq. 5).

The temporal evolution of the drop temperature in the sample experimental run of M-AL depicted in Fig. 3 can be described by the exponential decay function Eq. (B16) with $\tau = 11.3\,\mathrm{s}$, applying a ventilation coefficient of 5.6 which is in accord with the findings of Lierke (1995). The relaxation time τ was determined for each experimental run in M-AL and showed typical values between $8.94\,\mathrm{s}$ and $15.42\,\mathrm{s}$.

The actual cooling rate at a time instant during temperature adaptation is defined as $r(t) = -dT/dt$, that can be calculated after rearranging Eq. (18) to

$$T_a = T_e - (T_e - T_a(t=0))\exp\left(-t/\tau\right) \tag{19}$$

After some manipulation the actual cooling rate can be written as

$$r(T_a) = \frac{T_a - T_e}{\tau} \tag{20}$$

The $r(T_a)$ curve for $\tau = 11.3\,\mathrm{s}$ is shown in Fig. 4. It is apparent from the figure that at high temperatures the cooling rate is substantially high and gets moderate values only at low temperatures close to the equilibrium temperature. For such large cooling rates in M-AL measurements Eq. 13 predicts a significant shift in drop freezing temperature.
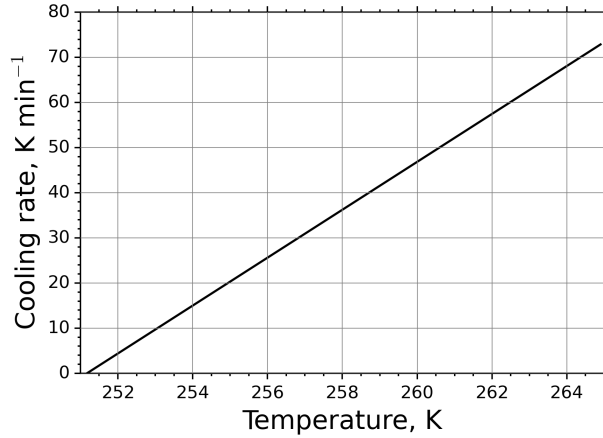
Figure 4. Actual cooling rate as the function of temperature in M-AL for the example shown in Fig. 3, with $\tau = 11.3\,\mathrm{s}$.

4 Results and Discussion

In this section we present the results of M-WT and M-AL experiments on immersion freezing using the clay mineral kaolinite. The data for other materials listed in Table 1 are presented in the Supplement Material.

4.1 M-WT experimental results

Figure 5 shows the INAS densities computed using Eq. (5) from f_{ice} spectra obtained from M-WT measurements of kaolinite with concentrations of $0.1\,\mathrm{g\,L^{-1}}$ and $1.0\,\mathrm{g\,L^{-1}}$ and marked with light and dark blue symbols, respectively. The number of data points is limited to five which is the issue of the M-WT experiments being very laborious for collecting statistically relevant numbers of measurements for each temperature. Comparing Fig. 5 with the INAS densities of other investigated materials presented in the Supplement reveals that kaolinite is a good atmospheric INP exhibiting large n_s values that, nevertheless, vary steeply over one order of magnitude within the investigated temperature range of only $4\,\mathrm{K}$, i.e. here from $252\,\mathrm{K}$ to $256\,\mathrm{K}$.

For computing n_s for Fig. 5 using Eq. (5), the fraction of frozen droplets f_{ice} was determined employing the singular approach, i.e. by counting the number of droplets frozen in an experimental run disregarding the time from injection until freezing. A droplet remaining liquid for up to 35 seconds (i.e. the end of the experimental run) was classified as unfrozen.

From the time resolved measurement data from M-WT, the time dependence of the freezing process was analysed. For that, Eq. (2) was rearranged to

$$\ln\left(\frac{n_{liq}(T,t)}{N_{tot}}\right) = -R(T) \cdot t \tag{21}$$

where $n_{liq}(T,t) = 1 - n_{fr}(T,t)$ is the number of droplets remaining liquid after time t at temperature T. Fig. 6 depicts the time dependence of liquid ratio from the M-WT measurements at five different temperatures and using the two distinct con-
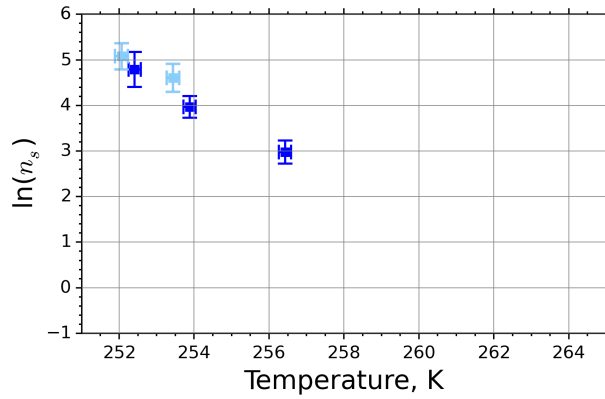
Figure 5. INAS density for kaolinite as function of temperature determined from the frozen fraction of $0.1\,\mathrm{g\,L^{-1}}$ and $1.0\,\mathrm{g\,L^{-1}}$ suspension drops (marked with light and dark blue, respectively) investigated in M-WT. Each data point represents 70 individually measured droplets, each of which with diameter of approximately 700 µm. The error bars are representing the 1σ values of the measured air temperatures and the calculated drop sizes.
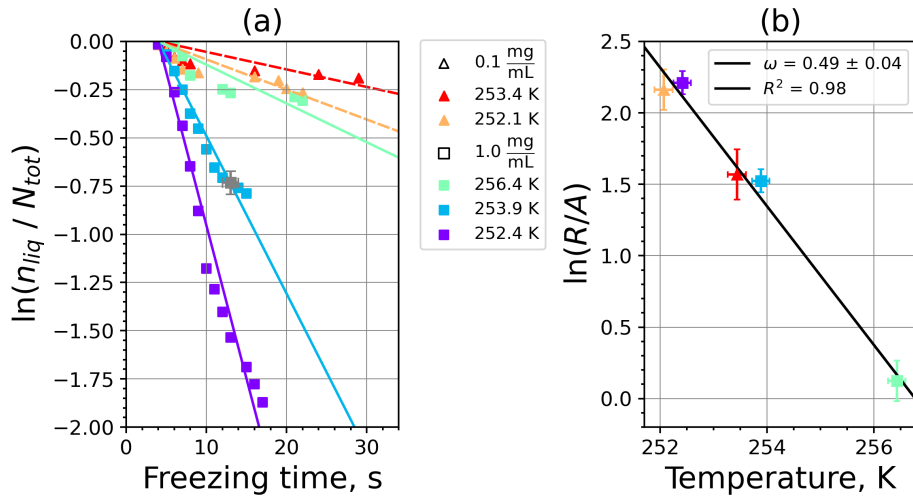
Figure 6. Kaolinite: (a) The decrease of fraction of droplets which remained liquid with time at different temperatures in the isothermal experiments in the M-WT. The colors are corresponding to different temperatures; experiments with particle concentrations of $0.1\,\mathrm{g\,L^{-1}}$ and $1\,\mathrm{g\,L^{-1}}$ are plotted by triangles and rectangles, respectively. The grey symbol marks a data point for $1\,\mathrm{g\,L^{-1}}$ at $253.9\,\mathrm{K}$ and indicates typical error bars. (b) Freezing rate of kaolinite normalized to surface area as function of temperature calculated from (a) using Eq. (21). The horizontal error bars are the 1σ values of the measured temperatures, while the vertical error bars are representing the fit error in R/A calculation.

centrations of kaolinite as for Fig. 5. The times needed for the injected droplets to reach their equilibrium temperatures (i.e. 6 seconds, see Fig. 2) were subtracted from the recorded time interval between injection and freezing. At lower temperatures and with higher particle surface areas per drop (i.e. higher INP concentration), the curves are getting steeper indicating that freezing proceeds faster. Fig. 6a clearly shows the expected exponential decay of liquid drops predicted by the stochastic approach. The temperature dependence of the normalized freezing rate according to Eq. (21) as shown in Fig. 6b was determined by computing the slopes of the curves in Fig. 6a and dividing them by the total surface areas of INP immersed in the examined water droplets. Fig. 6b reveals the expected linear dependency of R/A in agreement with Eq. 10. Hence, ω, which is the slope of R/A (see Eq. (10)), can readily be determined for the investigated kaolinite sample from Fig. 6b by linear regression as $\omega = 0.49 \pm 0.03$. (Here the error in ω is the standard error of the linear fit.) Note that if the INP can be considered as single-component, then $J_s = R/A$. In our experiments, the total surface area A was estimated from the concentration of the aqueous solution and from the specific surface area. To accurately measure the actual total surface area of INP inside the droplets, which should be taken into account for calculating ω and J_s, is currently not feasible. Therefore, the error of A might be significantly higher than estimated, which would result in a false classification of the INP as single-component.

4.2 M-AL experimental results

Frozen fractions of kaolinite suspension with $1.265\,\mathrm{g\,L^{-1}}$ concentration as function of temperature are shown in Fig. 7a. Error bars are associated to the temperature bin interval ($\pm 0.5\,\mathrm{K}$), and the uncertainty in the determination of f_{ice} stems from the counting statistics and the experimental temperature uncertainty. The active site density n_s calculated from Eq. 5 using f_{ice} in Fig. 7a is plotted in Fig. 7b. Here the error bars originate from Gaussian error propagation when using the measured data in Fig. 7a. From the calculation we excluded the data points for which f_{ice} was above 90% or below 10%. This cut-off was introduced because in these cases the uncertainty of f_{ice} was very large due to the poor counting statistics when freezing or unfreezing events occur very rarely.

Another criterion to use f_{ice} for further evaluations was that it should significantly exceed the background caused by impurities in the water used for generating the aqueous suspension. To determine this background spectrum, we investigated pure water droplets before each experimental run in M-AL, similarly to the M-WT measurements. However, in contrast to the findings for M-WT, some of the HPLC water droplets froze in M-AL. This indicates that the abundance of impurities in the HPLC water was high enough in the relatively large ($\sim 4\,\mu\mathrm{L}$) drops in M-AL to initiate freezing. Therefore, f_{ice} spectra for pure water samples were measured similarly as for the INP (Fig. 8). Although the number of freezing droplets was relatively small at temperatures higher than $248\,\mathrm{K}$, in some cases (e.g., when low concentrations were used) the INP nucleus spectra had to be corrected by considering the water background spectrum as described below.

In earlier experiments in M-AL (e.g., Diehl et al. (2014)), in-house produced MilliQ water was used as solvent for the aqueous solutions. Therefore, we also analyzed the MilliQ water in our present experiments. The results are plotted by black symbols in Fig. 8. Apparently, using HPLC water from a freshly opened chemical bottle (red symbols) reduces the background f_{ice}. Nevertheless, the f_{ice} spectrum of HPLC water changed with time and increased significantly after about a year (magenta symbols), indicating an aging effect. This behavior of different water types is in accord with the finding of Hiranuma et al.
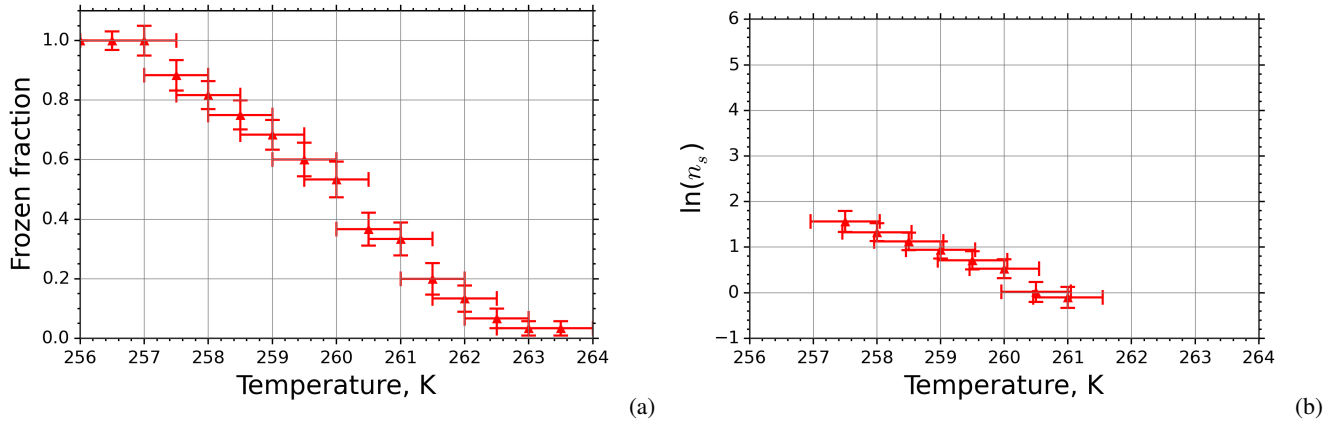
Figure 7. (a) Frozen fraction of $2\,\mathrm{mm}$ aqueous suspension droplets containing $1.265\,\mathrm{g\,L^{-1}}$ kaolinite measured in M-AL. (b) INAS density of kaolinite as function of temperature determined from the spectrum shown in (a).
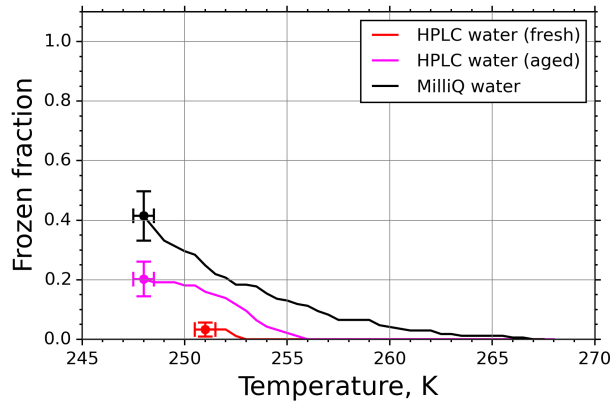
Figure 8. Freezing spectra of water of different purity grades: High precision liquid chromatography water (HPLC, SigmaAldrich), and in-house purified MilliQ water.

(2019). Since it is difficult to eliminate the contribution of INP still present in high purity water (see Fig. 8, and Whale et al. (2015), we applied a background correction method described below using the f_{ice} spectrum for pure water drops collected prior and during each set of experiments.

The background spectra were also corrected by shifting the freezing temperature following Vali (2014) with

$$\beta = 0.66\,\lg(r) \tag{22}$$

420

Although Vali proposed the factor 0.66 for the temperature correction of pure water, this parameter depends most probably on the type of impurities in the water. This is also suggested by Fig. 8 since the frozen fraction spectra are significantly different for different water samples, purity grades, and water age. Nevertheless, the temperature correction of Eq. 22 barely shifts the background spectra: $\beta = 0.46$ for $252\,\mathrm{K}$ where the cooling rate in M-AL is approximately $252\,\mathrm{K\,min^{-1}}$. Such a temperature shift would increase the background frozen fraction by less than 0.05. Therefore, no background subtraction (as, e.g., in Hader et al. (2014)) was applied but a cut-off temperature was defined where the difference between the background and the INP spectra was less than 0.05. This correction method was only necessary for FC and MCC in our experiments, while the other materials initiated freezing at higher temperatures for the investigated concentrations.

5   Reconciling the M-WT and M-AL experimental data by temperature correction

Plotting the INAS densities obtained from M-WT and M-AL experiments, respectively, in one figure reveals an apparent shift of the curves either in $\ln(n_s)$ or in the temperature (Fig. 9a). This shift was found for all investigated materials but with different magnitudes (s. Appendix A). Curves of INAS as function of temperature from the same experimental methods (M-AL or M-WT) but measuring different INP concentrations (s. Table 1) do not spread in such a systematic way, which indicates that the shift stems very likely from the detected freezing temperatures. Since M-AL exhibits a very large cooling rate for temperatures higher than $255\,\mathrm{K}$ (see Fig. 4), a temperature shift predicted by Eq. 13 can be significant for some given materials depending on their λ values. Nevertheless, we thoroughly checked other possible sources of any systematic freezing temperature shift. One obvious issue might arise from the relatively large volume of the drops examined in M-AL. In the experiments the surface temperature of the drops was continuously measured, however, if the drop cools down at a high rate, heat from the drop interior might not be transported outward sufficiently quickly. Some INP are located inside the drop, i.e. away from the drop surface, hence, they would experience higher temperatures than measured by the IR thermometer. This might falsify the experimentally determined temperature dependence of the ice nucleating ability. Nevertheless, our computation on the temporal evolution of a continuously cooling drop showed a temperature difference of maximum $0.5\,\mathrm{K}$ between the drop interior and surface which is within the measurement error of M-AL (s. Appendix B5). This temperature difference is higher at higher temperatures, where fewer freezing measurements were carried out. At surface temperatures below $258\,\mathrm{K}$ the difference is about $0.2\,\mathrm{K}$ only. Furthermore, the number of kaolinite particles in a $0.1\,\mathrm{g\,L^{-1}}$ aqueous suspension drop of $2\,\mathrm{mm}$ diameter, for instance, is approximately 300000. Thus, numerous particles will occur in the coldest region of the drop. Since a single particle is sufficient to initiate nucleation, the warmer temperature in the drop interior plays a minor role in initiating the freezing.

To modify the measurement data according to the temperature shift due to cooling rate and interparticle variability of ice nucleation efficiency, we follow the approach of Herbert et al. (2014) as described in Section 2. We present here only the case of kaolinite as an example; the approach was applied to reconcile the data for all examined materials. Those results are presented in Appendix A. The procedure for modifying for the raw data set in M-AL and M-WT is depicted as a flow diagram in Fig. B5.
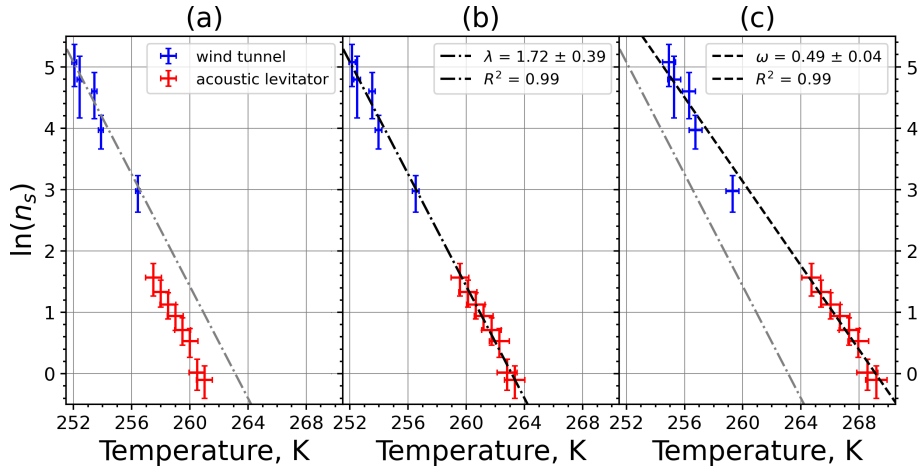
Figure 9. (a) Composite INAS density spectrum of kaolinite from the uncorrected M-WT (blue) and M-AL (red) measurements. (b) and (c) show the temperature-corrected data points from the M-WT and M-AL experiments based on λ and ω, respectively. The dashed-dotted line in (c) is the regression line for the corrected data points obtained by employing the optimal λ-value as in (b).

5.1 Determination of λ

The parameter λ for the temperature shift was determined assuming that with the correct λ value the $\ln(n_s)$ data from the two experiments M-WT and M-AL converge onto one single curve. Therefore, the temperatures of the unmodified data were shifted by applying Eq. (11) on the isothermal experimental data from M-WT, and Eq. (13) on the data obtained using continuous cooling approach of M-AL. For each investigated INP species a set of λ values varying from 0.1 to 8.0 in 0.1 steps applied for the modification in Eqs. (14) and (13). A linear fit to the derived $\ln(n_s)$ (black solid line and black data points in Fig. 10a) and the RMSE (root mean square error) between the data and the linear fit were calculated for each set of modified experimental data. The RMSE for the set of λ values for the kaolinite experiments is depicted in Fig. 10b. The optimal λ value, 1.7 in the present case, is corresponding to the minimum of the RMSE curve. This optimal value provides the best linear fit among the tested λs.

To determine the error of λ originating from the measurement error, the following procedure was used. We generated random data around each of the actually calculated n_s data points, but within the bounds of the measurement error (assuming the error bar of the measurement corresponding to 1σ). Hence, the number of data points for the λ-analysis did not change but each data point was shifted both in temperature and in n_s. Here, the distribution of n_s and T was not considered, random values within the error bounds were taken. Then, the optimal λ value for this modified data set was determined. We repeated this procedure 1000 times by generating new random data points, and from the statistical analysis of the obtained λ values, $\Delta\lambda$ was calculated. Choosing random values within the 1σ bounds around the mean data and neglecting values outside this bound might result in
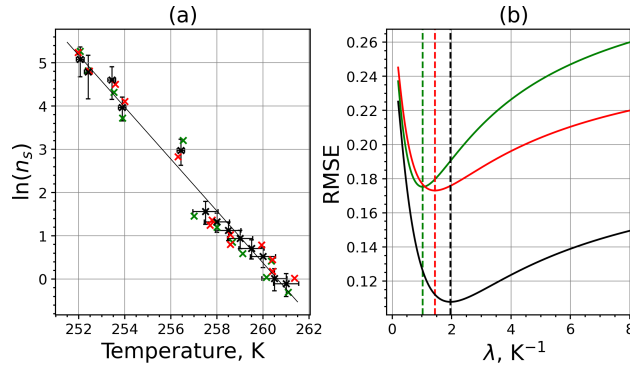
Figure 10. (a) Original (black; same as in Fig.9a), and two within the experimental error interval randomly generated data sets (red and green) using the measured INAS densities of kaolinite. The black solid line is the linear fit to the original experimental data set. (b) RMSE as the function of lambda for two of the 1000 randomly generated data sets. The vertical dashed lines indicate the optimal lambda values for the red, green and black curves.

470   overestimating $\Delta\lambda$. As an example for the procedure, two randomly generated data sets (plotted in red and green colors) and the corresponding RMSE values as function of lambda are shown in Figs. 10 a and b, respectively.

The optimal λ value of 1.7 was used to apply the temperature shift caused by the residence-time dependency of the freezing process in M-WT and by the cooling-rate dependency in M-AL. The modified data points together with the fitted regression line are plotted in Fig. 9b. When comparing Fig. 9b to Fig. 9a, the agreement between the modified data points from the two 475   distinct experimental methods is apparent. This is also supported by the high R^2 value of the regression line.

The temperature gradient of the normalized freezing rate, ω, was already determined in Section 4.1 from the time dependency of the frozen fraction measured in M-WT. The data points modified by the temperature shift Eq. (13) with presuming $\omega = \lambda$ are plotted in Fig. 9c together with the best fit line. Again, an obvious agreement can be seen between the two distinct experimental methods.

480   For a single-component INP, ω is equal to λ, which was found in Herbert et al. (2014) for their kaolinite sample from the Clay Mineral Society. In our study the $\omega = 0.49$ and $\lambda = 1.7$ values for our kaolinite sample from SigmaAldrich are differing. The deviation in the temperature correction based on λ and ω is further emphasized in Fig. 9c where the regression lines obtained by employing the optimal λ values and ω are plotted by dash-dotted and dashed lines, respectively. This plot suggests that the kaolinite sample investigated in our study has to be treated as a multi-component system, and the determined λ-value 485   should be employed for modifying the measured freezing temperatures.

The ω and λ values for the investigated materials are listed in Table 3. After definition of Vali (1994) and Herbert et al. (2014), all materials exhibit multiple-component behaviour since $\omega < \lambda$ in all cases. Nevertheless, for some materials, e.g., illite NX, despite different λ and ω values the deviation between the data sets modified using λ or ω was not obvious (see Appendix A). To obtain further insights in this feature, we performed statistical significance tests as follows.

Table 3. λ and ω values, and the classification of the investigated materials. The results of statistical t-tests are also given: calculated t-values, number of samples (data points), and t-values showing significance in $\alpha = 99.5\%$.

Material	λ in K^{-1}	ω in K^{-1}	$t_{s,\omega}\,\lvert$	$t_{s,\lambda}\,\lvert\,N\,\lvert\,t_{sig}$	Single/Multiple component
FC	2.61 ± 0.25	1.41 ± 0.33	$3.43\rvert$	$3.72\lvert 26\rvert 3.725$	Single
MCC	1.57 ± 0.04	1.29 ± 0.21	$-3.02\rvert$	$-2.03\lvert 12\rvert 4.437$	Single
Feldspar	1.17 ± 0.07	0.65 ± 0.09	$10.06\rvert$	$10.15\lvert 39\rvert 3.566$	Multiple
Illite NX	1.46 ± 0.20	0.87 ± 0.16	$2.54\rvert$	$3.08\lvert 28\rvert 3.689$	Single
Kaolinite	1.72 ± 0.39	0.49 ± 0.03	$11.48\rvert$	$26.97\lvert 13\rvert 4.318$	Multiple
Montmorrilonite K10	1.43 ± 0.21	0.66 ± 0.15	$5.46\rvert$	$7.03\lvert 26\rvert 3.725$	Multiple
Sahara dust SDB01	1.21 ± 0.23	0.84 ± 0.09	$4.31\rvert$	$5.73\lvert 16\rvert 4.073$	Multiple

First, we computed the arithmetic mean curve of the two best fit lines corresponding to λ and ω, respectively, and calculated their mean deviation $\bar{d}$ from that mean curve. The ultimate question of our statistics tests was, whether the mean deviation is significant with respect to the measurement error and data scatter. Hence, as the next step, the error weighted standard deviations of the residuals s_ω and s_λ were calculated as

$$s_\omega = \sqrt{\frac{\sum_{i=1}^{N} \frac{\left(\Delta_{\omega,i} - \overline{\Delta_\omega}\right)^2}{\Delta T_i^2}}{\sum_{i=1}^{N} \frac{1}{\Delta T_i^2}}} \tag{23}$$

$$s_\lambda = \sqrt{\frac{\sum_{i=1}^{N} \frac{\left(\Delta_{\lambda,i} - \overline{\Delta_\lambda}\right)^2}{\Delta T_i^2}}{\sum_{i=1}^{N} \frac{1}{\Delta T_i^2}}} \tag{24}$$

where ΔT_i is the temperature measurement error, $\Delta_{\omega,i}$ and $\Delta_{\lambda,i}$ are the deviations of the corrected data points from the corresponding best fit curves, while $\overline{\Delta_\omega}$ and $\overline{\Delta_\lambda}$ are the mean values of these deviations. For the significance test we applied a two-sided Student t-test on a significance level of 99.9%, and calculated

$$t_{s,\omega} = \frac{\lvert \bar{d} - \mu_0 \rvert}{s_\omega} \cdot \sqrt{N} \tag{25}$$

$$t_{s,\lambda} = \frac{\lvert \bar{d} - \mu_0 \rvert}{s_\lambda} \cdot \sqrt{N} \tag{26}$$

where N is the number of data points. The null hypothesis was that the two linear curves do not significantly differ, thus, $\mu_0 = 0$ for their deviation from the arithmetic mean curve. In Table 3 we listed the calculated $t_{s,\omega}$ and $t_{s,\lambda}$, the number of data points, and the tabulated t_{sig} ($\beta = 99.9\%$) values for the Student t-test for each material. If $t_{s,\omega}$ or $t_{s,\lambda}$ is greater than t_{sig}

($\beta = 99.9\%$), then the null hypothesis is rejected. That means that the two best fit lines are differing significantly with respect to data scatter and measurement error, and consequently, the material is treated as multiple component on a 99.9% confidence level. Otherwise we consider the material as single component albeit the statistical test does not prove the null hypothesis. Hence, we classify the material as single or multiple component within our measurement error and data scatter.

As listed in Table 3, according to our statistical test kaolinite, feldspar, montmorillonite, and Sahara dust are multiple-component, while illite NX, FC, and MCC are single-component INP. This implies that the definition of Herbert et al. (2014) to distinguish between single and multiple component samples on the basis of λ and ω values cannot directly be adapted to our M-AL and M-WT experiments. This is the consequence of the adaptive cooling of the drops in M-AL which results in a temperature dependence in the λ based correction. Thus, the same λ value caused a higher temperature correction at higher temperatures (see Fig. B4 in the Appendix). Therefore, our analysis indicates that statistic tests have to be performed considering both data scatter and measurement error to compare the λ and ω values. This procedure improves the classification of the materials as single or multiple component.

The statistical tests supported that the kaolinite that we analysed is multiple component. That contradicts the finding of Herbert et al. (2014) who showed their kaolinite sample (KGa-1b from the Clay Mineral Society) to be single component with $\lambda = \omega = 1.12$. This indicates that these two kaolinite samples are different and, thus, the result outputs cannot directly be compared since the IN activity of materials depends on their specific chemical composition, which is known to be very variable for kaolinite. For example, the λ value for the kaolinite used in the cooling experiments of Wright and Petters (2013) was 1.7, which is equal to our result. In contrast, the Fluka kaolinite sample measured by Welti et al. (2012), which is known to contain particles of very ice active feldspar, had a λ value of 2.2 (see Table 2 in Herbert et al. (2014)). In general, we found slightly higher λ values for biological aerosols (FC and MCC) than for mineral dusts. This results in smaller ΔT in Eq. (9), and hence, biological INP show a weaker time dependence, in agreement with the findings of Peckhaus et al. (2016) and Budke and Koop (2015). The temperature correction ranged for the investigated samples in our experiments from $\approx 0.5\,\mathrm{K}$ up to several Kelvins, depending on the material's λ-value (see also Fig. B4 in the Appendix).

The composite plot of the INAS densities for all investigated materials obtained by M-WT and M-AL measurements is shown in Fig. 11. In accord with the literature (e.g., Atkinson et al. (2013)), feldspar is far the most efficient ice nucleating particle type among the investigated dust materials. Besides feldspar, kaolinite has also a high IN efficiency, in particular at higher temperatures. The biological particles (FC, MCC) and the clay minerals illite NX and Sahara dust have similar temperature dependent n_s values. The one exception is montmorillonite, which was found to be the least efficient within the investigated temperature range from $248\,\mathrm{K}$ to $266\,\mathrm{K}$. In Fig. 11 also shown are parameterizations for feldspar (Atkinson et al., 2013) and for desert dust (Ullrich et al., 2017). Our temperature corrected feldspar data fits very well to the parameterization of Atkinson et al. (2013) which was based on cold stage experiments, i.e. using aqueous suspensions of INP material. In contrast, the desert dust parameterization of Ullrich et al. (2017) is based on dry deposition experiments and predicts higher INAS densities as measured in M-WT and M-AL. This is in accord with the literature, as for example Hiranuma et al. (2019) revealed different INAS densities when dry deposition or aqueous suspension techniques were utilized.
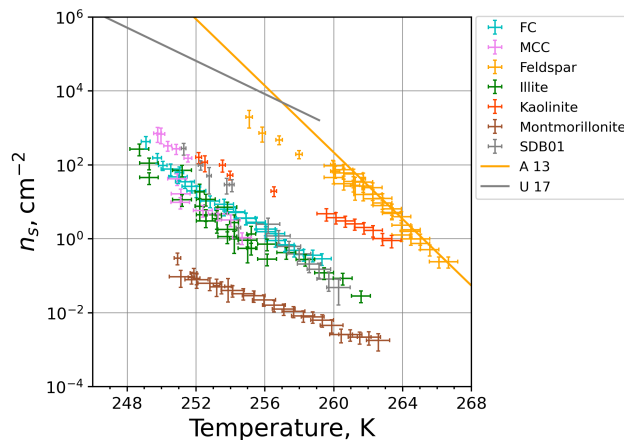
Figure 11. INAS densities of the investigated materials as function of temperature. The data points are composites from M-WT and M-AL measurements and are corrected for the cooling rate. Orange and gray solid lines show parameterizations for feldspar (Atkinson et al., 2013) and desert dust (Ullrich et al., 2017), respectively.

6   Conclusions and Suggestions

Immersion freezing efficiencies of different types of aerosol particles such as pure and natural clay minerals as well as biologi-
540   cal particles, were studied using two distinct measurement techniques, an acoustic levitator (M-AL) and a vertical wind tunnel (M-WT). Both instruments utilize freely floating of individual droplets.

The INAS densities of different types of aerosol particles obtained by M-AL and M-WT revealed a shift in the freezing temperatures to lower values. Such a shift in freezing temperatures became obvious in our earlier experiments in the measurement campaigns FIN02 (DeMott et al., 2018) and INUIT-cellulose (Hiranuma et al., 2019). Therefore, we had already corrected the
545   data published in those papers for the freezing temperature shift. Following the procedure depicted in Fig. B5, we were able to bring the INAS densities obtained from the two different methods in line. We have also reconciled our earlier experiments on illite NX (Diehl et al., 2014) and ascertained that those data were burdened with a temperature shift as well. A modification of the data in Diehl et al. (2014) according to our new findings improves further the agreement of the data from M-WT and M-AL (green symbols in Fig. 11).

550   Taking advantage of having two independent single droplet levitation methods located in our laboratory we determined the material dependent λ value which determines the temperature shift due to cooling rate for the investigated aerosol types based on the analysis method suggested by Herbert et al. (2014). Furthermore, we classified the aerosol materials investigated in this study as single- or multiple-component, i.e. whether their nucleation process shows weak or strong time dependence. This result has a direct impact on the applicability of the singular approach on the evaluation of data from immersion freezing with various
555   INP types, i.e. whether the time-dependence of freezing can be neglected or not. Further, if an INP type is single-component, the temperature shift can ultimately be calculated from the gradient of the measured freezing rate ω.

An important conclusion on the applicability of laboratory immersion freezing techniques can be made due to the different air flow conditions applied in our experiments. In M-WT a continuous air flow is established around a floating droplet (correctly simulating the real atmospheric condition), whereas M-AL maintains levitation with a very weak air flow. Since the INAS densities obtained by M-WT and M-AL after applying the temperature shift due to the cooling rate show very good agreement, one can conclude that the air flow around the droplets containing the INP does not significantly influence the immersion freezing process.

Based on the experiences collected during the presented synergetic study we suggest the following points for future immersion freezing studies:

- If the instrument used for the measurements utilizes a continuously varying cooling rate, then its temperature adaptation decay has first to be characterized in terms of equilibrium temperature and decay constant and the corresponding uncertainties. Furthermore, the drop temperature has to be measured directly, because it can significantly deviate from the ambient temperature.

- When comparing the IN efficiencies measured by different instruments utilizing distinct cooling rates, the comparison has to be carried out very carefully and critically. We suggest using the same or at least similar cooling rates in the different instruments in such intercomparison studies.

- We note from Fig. 8 that freezing behavior and, consequently, the necessity of background correction depends on the purity grade and age of water used for producing aqueous suspension samples. Therefore, it has to be carefully characterized for all experiments as well.

- In case the INAS densities are measured applying a non-standard cooling rate (i.e. $CR \neq 1\,\mathrm{K\,min^{-1}}$), the freezing temperatures have to be corrected following the procedures of Herbert et al. (2014) and the one described in this study. It has to be taken into account that the temperature shift is material-dependent and most probably temperature dependent for most of the INP.

- By the characterization of the aerosol material in terms of a temperature shift due to changes in the cooling rate, statistical significance tests should be carried out taking both the data scatter and the measurement error into account. Of course, by increasing the measurement sensitivity (i.e. decreasing the measurement error) or by decreasing the data scatter (either by improving the measurement accuracy or due to a reduced natural variability of the sample material), the prediction whether the ice nucleation of the material can be described using a single or a multiple component model will be more accurate. Nevertheless, the classification can only be obtained within the measurement error and accuracy of the applied experimental method.

- In cloud models the cooling rate has to be considered and the freezing temperatures of materials have to be corrected taking the material dependent λ values into account.

- It has to be emphasized that the total surface area of the particles in the individual droplets is a crucial parameter for the procedure described in this paper (see Eq. (5)). It can vary, for instance, with sample particle size distribution or due to aggregation inside the droplets. It should be determined in each droplet under investigation which seems currently not feasible. In our study we estimated the total surface area from the concentration of our aqueous solutions and from the specific surface areas of the materials. Alternatively, size-selected particles might be used for the immersion freezing measurements which would decrease the surface area uncertainty (Alpert and Knopf, 2016) and improve the analysis conducted here. We also note that the model calculations of Alpert and Knopf (2016) concluded that the assumption of identical particle surface area in the droplets imposes a cooling rate dependence on J_s which was not the case in our considerations. Based on these calculations, Knopf et al. (2020) demonstrated that surface area variance and stochasticity explains the freezing of illite NX. Furthermore, as demonstrated by Barahona (2020), composition and surface area variation between INP may introduce biases in calculated $n_s(T)$ and $J_s(T)$, implying the necessity of the accurate determination of these quantities in laboratory immersion freezing experiments. The variability of particle surface area from droplet to droplet in our M-WT measurements might cause the non-linear behaviour of $\ln(n_{liq}/N_{tot})$ for some INP materials (see Appendix).

- The λ parameter and the temperature shifts of some aerosol species determined by Herbert et al. (2014) and in the present study serve rather for orientation. We suggest the determination of such temperature shifts for the specific material samples under investigation in each future experimental study on immersion freezing of aerosol particles. Variations in chemical composition, ageing, sample contamination, and others can result in changes of λ.

Data availability. The data set used for generating the figures is available under https://doi.org/10.5281/zenodo.4436153. The raw measurement data will be provided upon request.

Video supplement. A video supplement showing the record of the immersion freezing of a liquid drop in the M-AL can be downloaded from https://doi.org/10.5446/46729

 Appendix A: Further reconciled experimental results

In this section we provide the experimental results for the determination of the temperature dependent freezing rate (as in Fig. 6), as well as the composite INAS density spectra from M-WT and M-AL using λ and ω (as in Fig. 9) for the materials listed in Table 1.

A1 Fibrous cellulose (FC)
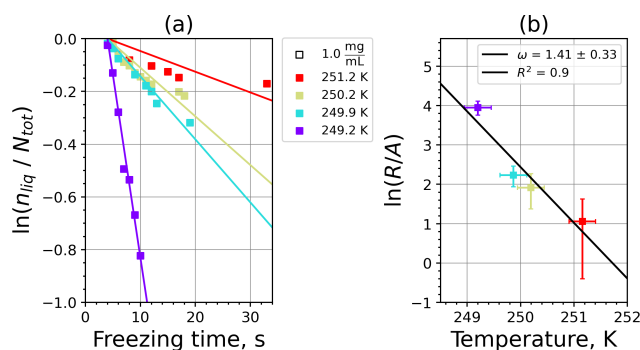
Figure A1. (a) The decrease of fraction of droplets which remained liquid with time at different temperatures in the isothermal experiments of fibrous cellulose (FC) at the M-WT. The colors are corresponding to different temperatures (particle concentrations $1 \, \mathrm{g \, L^{-1}}$). Typical error bars are depicted in Fig. 6. (b) Freezing rate of FC normalized to surface area as function of temperature.
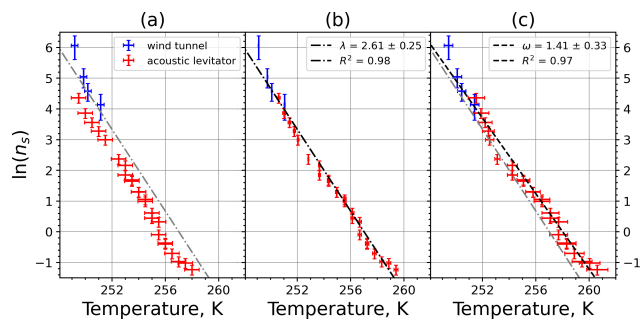
Figure A2. (a) Composite INAS density spectrum of FC from the uncorrected M-WT (blue) and M-AL (red) measurements. (b) and (c) show the temperature corrected data points from the M-WT and M-AL experiments based on λ and ω, respectively. The dash-dotted line in (c) is the regression line on corrected data points obtained by employing the optimal λ-value as in (b).
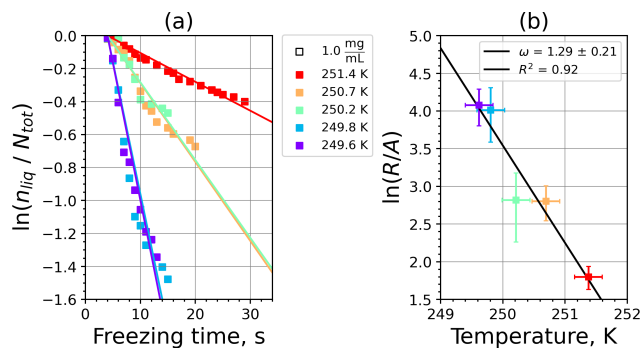
Figure A3. (a) The decrease of fraction of droplets which remained liquid with time at different temperatures in the isothermal experiments of microcrystalline cellulose (MCC) at the M-WT. The colors are corresponding to different temperatures (particle concentrations $1\,\mathrm{g\,L^{-1}}$). Typical error bars are depicted in Fig. 6. (b) Freezing rate of MCC normalized to surface area as function of temperature.
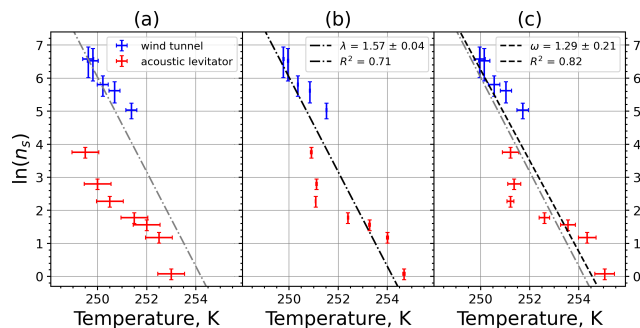
Figure A4. (a) Composite INAS density spectrum of MCC from the uncorrected M-WT (blue) and M-AL (red) measurements. (b) and (c) show the temperature corrected data points from the M-WT and M-AL experiments based on λ and ω, respectively. The dash-dotted line in (c) is the regression line on corrected data points obtained by employing the optimal λ-value as in (b).
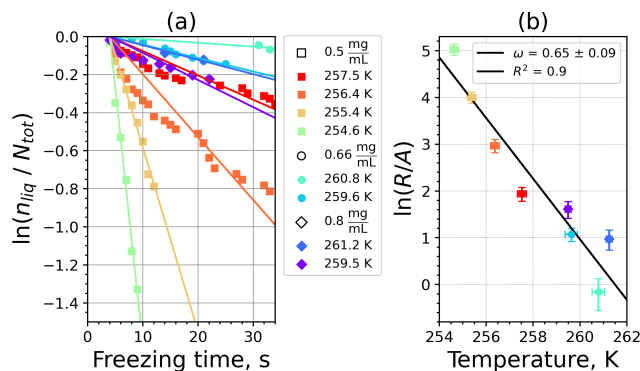
A3 Feldspar

Figure A5. (a) The decrease of fraction of droplets which remained liquid with time at different temperatures in the isothermal experiments for feldspar at the M-WT. The colors are corresponding to different temperatures; experiments with particle concentrations of $0.5\,\mathrm{g\,L^{-1}}$, $0.66\,\mathrm{g\,L^{-1}}$, and $0.8\,\mathrm{g\,L^{-1}}$ are plotted by rectangles, circles and triangles, respectively. Typical error bars are depicted in Fig. 6.(b) Freezing rate of feldspar normalized to surface area as function of temperature.
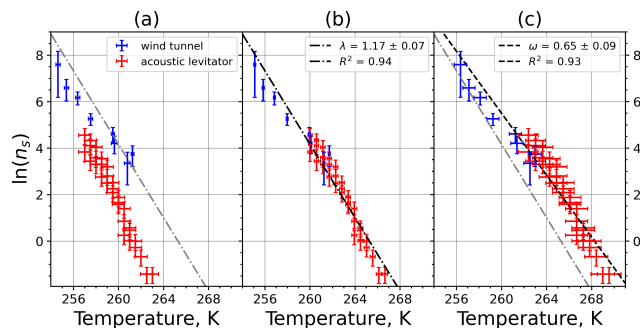
Figure A6. (a) Composite INAS density spectrum of feldspar from the uncorrected M-WT (blue) and M-AL (red) measurements. (b) and (c) show the temperature corrected data points from the M-WT and M-AL experiments based on λ and ω, respectively. The dash-dotted line in (c) is the regression line on corrected data points obtained by employing the optimal λ-value as in (b).
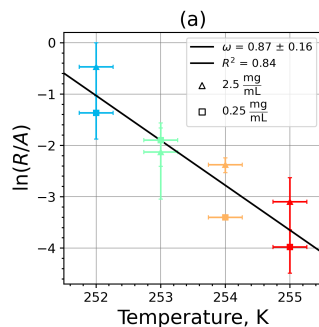
A4 Illite NX

Figure A7. Freezing rate of illite NX normalized to surface area as function of temperature for experiments at the M-WT with particle concentrations of $2.5\,\mathrm{g\,L^{-1}}$ and $0.25\,\mathrm{g\,L^{-1}}$ (plotted by triangles and rectangles, respectively). Freezing rates were calculated from the time dependence of the liquid ratio of illite NX presented in Fig. 6. in Diehl et al. (2014).
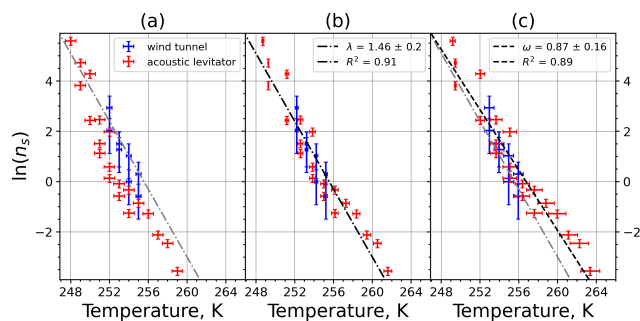
Figure A8. (a) Composite INAS density spectrum of illite NX from the uncorrected M-WT (blue) and M-AL (red) measurements. (b) and (c) show the temperature corrected data points from the M-WT and M-AL experiments based on λ and ω, respectively. The dash-dotted line in (c) is the regression line on corrected data points obtained by employing the optimal λ-value as in (b).
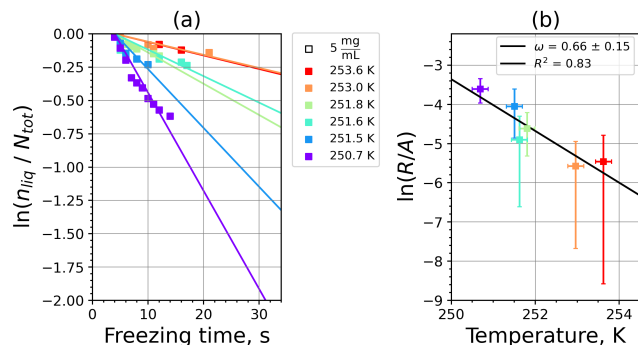
A5 Montmorilonite

Figure A9. (a) The decrease of fraction of droplets which remained liquid with time at different temperatures in the isothermal experiments for montmorillonite at the M-WT. The colors are corresponding to different temperatures (particle concentrations $5\,\mathrm{g\,L^{-1}}$). Typical error bars are depicted in Fig. 6.(b) Freezing rate of montmorillonite normalized to surface area as function of temperature.
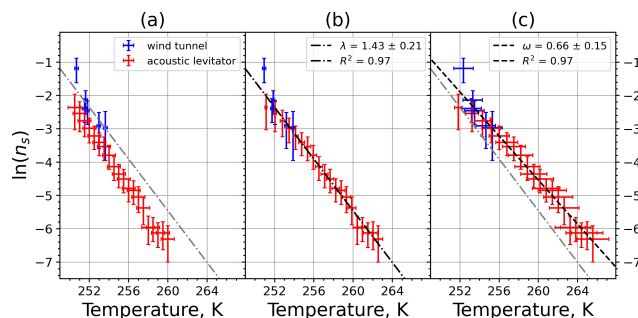
Figure A10. (a) Composite INAS density spectrum of montmorillonite from the uncorrected M-WT (blue) and M-AL (red) measurements. (b) and (c) show the temperature corrected data points from the M-WT and M-AL experiments based on λ and ω, respectively. The dash-dotted line in (c) is the regression line on corrected data points obtained by employing the optimal λ-value as in (b).
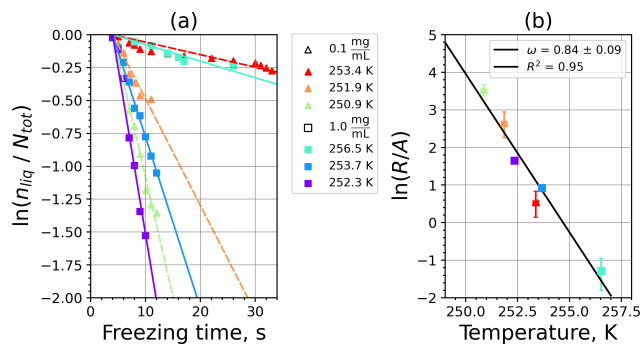
Figure A11. (a) The decrease of fraction of droplets which remained liquid with time at different temperatures in the isothermal experiments for Sahara dust at the M-WT. The colors are corresponding to different temperatures (particle concentrations $5\,\mathrm{g\,L^{-1}}$). Typical error bars are depicted in Fig. 6.(b) Freezing rate of Sahara dust normalized to surface area as function of temperature.
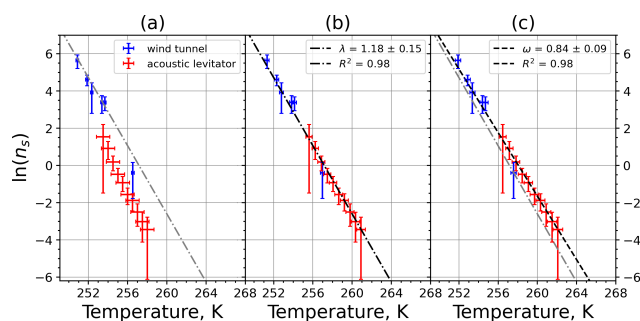
Figure A12. (a) Composite INAS density spectrum of Sahara dust from the uncorrected M-WT (blue) and M-AL (red) measurements. (b) and (c) show the temperature corrected data points from the M-WT and M-AL experiments based on λ and ω, respectively. The dash-dotted line in (c) is the regression line on corrected data points obtained by employing the optimal λ-value as in (b).

Appendix B: Drop temperature adaptation in the M-AL and in the M-WT

A liquid droplet placed in a colder or warmer environment tends to a quasi-steady state temperature difference between itself and its surrounding. In order to describe the temperature adaptation process, diffusional and convective heat and mass transfers for water vapor are considered. We will follow the concept of Pruppacher and Klett (2010) in the forthcoming derivation. Hence, first, the heat and mass transfer of a motionless droplet will be described, and after that the effect of air ventilation will be introduced. The symbols used here are listed in the List of Symbols.

B1   Diffusional heat and mass transfer of a motionless drop in equilibrium

When computing the simple case of the diffusional heat transfer of a motionless water droplet in air latent heat from condensation or evaporation is not considered. The rate of heat is calculated by integrating the heat flux density over the entire droplet surface. The heat flux density can be derived from Fourier's law which in spherical coordinates reads as

$$j_{h,r}|_{r=a} = -k_a \left(\frac{\partial T}{\partial r} \right)_{r=a} \tag{B1}$$

where r is the distance from the drop center. Thus, the rate of heat transfer of a motionless drop considering pure diffusional heat transfer is

$$\left(\frac{dq}{dt} \right)_0 = -k_a \int_S \left(\frac{\partial T}{\partial r} \right)_{r=a} dS \tag{B2}$$

The temperature is determined by solving the heat conduction equation which has its form in spherical coordinates for a motionless drop under steady state thermal condition:

$$\frac{\partial^2 T}{\partial r^2} + \frac{2}{r} \frac{\partial T}{\partial r} = 0 \tag{B3}$$

This partial differential equation is solved using the boundary conditions:

$$T(r = \infty) = T_\infty \tag{B4}$$

$$T(r = a) = T_a \tag{B5}$$

where T_∞ is the temperature in the free air, i.e. far away from the drop; and T_a is the drop surface temperature, while a is the drop radius. The solution for the temperature as function of r is

$$T(r) = T_\infty + (T_a - T_\infty) \frac{a}{r} \tag{B6}$$

Hence,

$$\left(\frac{dq}{dt} \right)_0 = 4\pi a k_a (T_\infty - T_a) \tag{B7}$$

Similarly to the heat transfer, the mass transfer rate of an motionless droplet in equilibrium with its surrounding air is calculated from

$$\left(\frac{dm}{dt} \right)_0 = -D_v \int_S \left(\frac{\partial \rho_v}{\partial r} \right)_{r=a} dS \tag{B8}$$

where D_v is the water vapor diffusion coefficient, and ρ_v is the water vapor density in the surrounding air around the water droplet. The water vapor density can be found by solving the convective diffusion equation:

$$\frac{\partial \rho_v}{\partial t} + \nabla \rho_v u = D_v \nabla^2 \rho_v \tag{B9}$$

This differential equation simplifies for a motionless drop in steady state to Laplace's equation in the form: $\nabla^2 \rho_v = 0$ (cf. B3).The boundary conditions for the problem are

$$\rho_v(r = \infty) = \rho_{v,\infty} \tag{B10}$$

$$\rho_v(r = a) = \rho_{v,a} \tag{B11}$$

where $\rho_{v,\infty}$ and $\rho_{v,a}$ are the water vapor densities in the air far away from the drop and at the drop surface, respectively. The solution of the governing differential equation is similar to that for the heat transfer. Thus, the rate of change of the mass of a motionless droplet due to diffusion of water vapor under steady state conditions is given by

$$\left(\frac{dm}{dt}\right)_0 = 4\pi D_v \left(\rho_{v,\infty} - \rho_{v,a}\right) \tag{B12}$$

B2   Heat and mass transfer of an evaporating drop in air flow

We now consider the more realistic and atmospherically relevant case involving also the effect of air motion around the droplet The total rate at which a drop falling in air gains heat is the sum of the convective heat flux from the air to the drop and the heat loss of the drop by releasing latent heat due to evaporation:

$$\left(\frac{dq}{dt}\right)_a = 4\pi a k_a \left(T_\infty - T(t)\right) \cdot f_h + L_e \frac{dm}{dt} \cdot f_v \tag{B13}$$

where the so called ventilation coefficients f_h and f_v are introduced accounting for the enhanced heat and mass transfer, respectively, due to ventilation. Thus, for a drop in an air flow $f_h > 1$ and $f_v > 1$, while a motionless evaporating drop can be described using Eq. (B13) by setting $f_h = 1$ and $f_v = 1$. In M-AL or in M-WT where a warm ($\approx 20\,^\circ$C) drop is injected into a cold subsaturated environment, both terms on the right hand side of Eq. (B13) are negative. The drop cools down at a rate proportional to its mass m determined by

$$\left(\frac{dq}{dt}\right)_a = mc_w \frac{d}{dt}\left(T_a - T_\infty\right) \tag{B14}$$

where c_w is the specific heat capacity of water. By equating Eqs. (B13) and (B14) we get the governing equation for the temperature adaptation of the droplet as

$$\frac{4\pi}{3} a^3 \rho_w c_w \frac{d}{dt}\left(T_\infty - T_a(t)\right) = -4\pi a k_a \left(T_\infty - T_a(t)\right) \cdot f_h$$
$$- 4\pi a L_e D_v \left(\rho_{v,\infty} - \rho_{v,a}\right) \cdot f_v \tag{B15}$$

After integration, we obtain the following solution of this differential equation:

675 $$T_\infty - T_a(t) - \delta = (T_\infty - T_a(t=0) - \delta)\exp(-t/\tau) \tag{B16}$$

with the time constant

$$\tau = \frac{a^2 \rho_w c_w}{3\left[k_a L_e D_v \left(\frac{d\rho_v}{dT}\right)_{sat}\right] \cdot f_h} \tag{B17}$$

and

$$\delta = \frac{D_v L_e f_v \left[\frac{1-r_v}{r_v}\rho_{v,\infty}\right]}{k_a \cdot f_h + L_e D_v f_v \left(\frac{d\rho_v}{dT}\right)_{sat}} \tag{B18}$$

680 which gives the steady temperature difference between the equilibrium temperature ($T_e = T_a(t \to \infty)$) of a ventilated evapo-rating drop and its surrounding air at a relative humidity of r_v. For simplicity we did not indicate but the physical quantities are represented by their averages over the integration interval. Furthermore, we assumed that $f_h = f_v$ (Pruppacher and Klett, 2014).

After some manipulation, and using $\rho_{v,sat}(T_e) = \rho_{v,a}(T_e)$ one can get two other forms for δ:

685 $$\delta = \frac{D_v L_e f_v \left[\rho_{v,sat}(T_e) - \rho_{v,\infty}\right]}{k_a \cdot f_h} \tag{B19}$$

or, by applying the ideal gas law

$$\delta = \frac{D_v L_e f_v}{k_a \cdot f_h} \frac{M_w}{R}\left(\frac{e_{sat}(T_e)}{T_e} - \frac{e_\infty}{T_\infty}\right) \tag{B20}$$

where $e_{sat}(T_e)$ is the saturation water vapor pressure at temperature T_e, and e_∞ is the water vapor pressure in the air. Hence, the equilibrium drop temperature is given as

690 $$T_e = T_\infty - \frac{D_v L_e f_v}{k_a \cdot f_h} \frac{M_w}{R}\left(\frac{e_a(T_e)}{T_e} - \frac{e_\infty}{T_\infty}\right) \tag{B21}$$

In M-AL the levitating drop may gain heat from the absorbed acoustic energy at a certain constant rate:

$$\frac{dq_{ac}}{dt} = e_{ac}V \tag{B22}$$

where e_{ac} is the acoustic energy density flux and V is the drop volume. e_{ac} varies with time at a very high frequency (≈ 20 kHz) therefore it can be considered as time independent when discussing the slow process of heat transfer. Since this term

695 is independent on temperature and time, it does not affect τ and will not appear in Eq. (B17), which describes the time dependence of the temperature adaptation process. Nevertheless, the absorbed acoustic energy heats up the drop and increases δ with a constant temperature value. This temperature difference between the theoretically calculated equilibrium temperature and the environmental temperature was also observed in M-AL, and calculated to be $\approx 4.5K$.

B3 Drop surface temperature in M-AL

700 Although there is seemingly no air flow around a drop levitating in M-AL, the pressure distribution caused by the acoustic waves does create convection about it (Lierke, 1995). This has to be considered in the temporal evolution calculation in Eq. (B17). In Fig. B1 an example of the measured surface temperature evolution of a 2-mm diameter drop placed into M-AL is plotted by black line. Neglecting ventilation around the drop (i.e. $f_v = 1.0$ in Eq. (B17)) the cooling would be much slower (blue line) than in reality. Setting the ventilation coefficient to $f_v = 5.2$ - which value is close to $f_v = 3$ determined by Lierke

705 (1995) - the temperature evolution follows accurately the measured curve (green line).
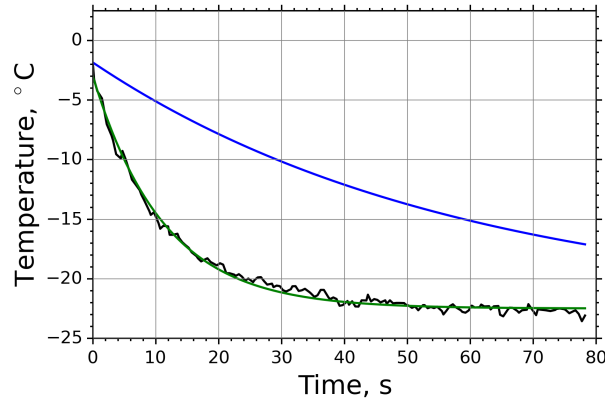
Figure B1. Temporal evolution of the surface temperature of a 2-mm diameter drop injected into M-AL: measured (black line); calculated using Eq. (B16) without ventilation (blue line); calculated using Eq. (B16) with a ventilation factor $f_v = 5.2$ (green line).

B4 Internal drop temperature simulation in M-AL

In M-AL experiments the continuous sharp surface temperature drop caused by the adaptation to the significantly colder environment results in a temperature difference in the drop interior. Therefore, the temperature at the drop surface is lower than close to the drop center. Since the drop temperature was determined in the M-AL experiments by measuring the surface

710 temperature by means of an infrared thermometer, the actual (internal) temperature experienced by ice nucleating particles inside the drop is higher than the measured value. This measurement artifact might falsify the experimentally determined temperature dependence of the ice nucleating ability. In order to estimate this experimental issue, a simulation was carried out based on the theoretical formulation of the temperature adaptation given above and on heat conduction inside the liquid drop. The drop volume was split into 10 layers of equivalent radii and the heat conduction among the layers was calculated by

715 solving the transient heat equation

$$\frac{\partial T}{\partial t} = \frac{\partial^2 T}{\partial r^2} + \frac{2}{r}\frac{\partial T}{\partial r} \tag{B23}$$

For the numerical integration explicit finite difference method was used. During the simulation the surface temperature was continuously cooling following the experimentally obtained adaptation curve shown in Fig. B1. The temperature distribution inside the drop is depicted at four time instances (i.e. drop surface temperatures) in Fig. B2 revealing the temperature difference between the drop surface and the drop center.
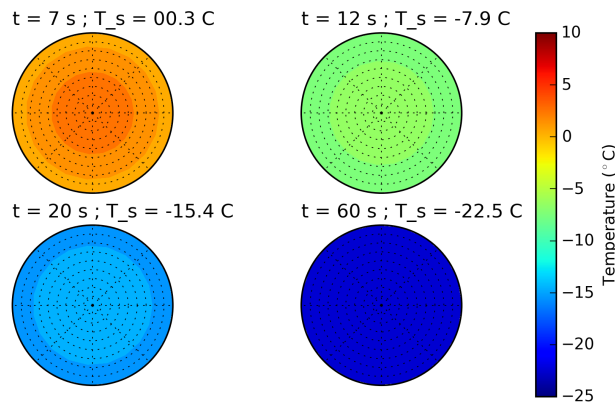
Figure B2. Internal temperatures at four different time instances for a continuously cooling drop of 2 mm diameter in M-AL following Fig. B1, based on numerical simulation of the heat conduction equation.

The temperature variation of three layers together with the volume averaged drop temperature change relative to the surface temperature are further investigated in Fig. B3. While the temperature at drop's center (red curve) deviates from the surface temperature by up to $2.5\,^{\circ}$C, the second outmost layer representing 40% of the entire drop volume (green curve) follows the surface temperature within $0.5\,^{\circ}$C at subzero temperatures. At temperatures below $-5\,^{\circ}$C, which are relevant for immersion freezing experiments, the temperature difference is less than $0.3\,^{\circ}$C, thus, within the measurement uncertainties. The volume averaged drop temperature (magenta curve in Fig. B3) is also within the measurement uncertainty of $0.5\,^{\circ}$C for this temperature range.

The simulation was carried out without considering any internal circulation, which would further and faster unify the temperature distribution inside the liquid. Considering the large number of ice nucleating particles ($\gtrsim 300.000$) immersed in each of the drops, one can conclude, that the surface temperature measured by the pyrometer can be used as characteristic drop temperature.

The temperature difference between the surface and the volume average temperature of the drop is compared to the temperature shift calculated for three different λ values in Fig. B4. The figure reveals that the calculated temperature difference inside the drop (magenta curve) is a factor of 6 to 20 smaller than the temperature shift caused by the high cooling rate in M-AL for different λ values (red, green, and blue lines). Therefore, this effect cannot explain the observed freezing temperature shift in M-AL.
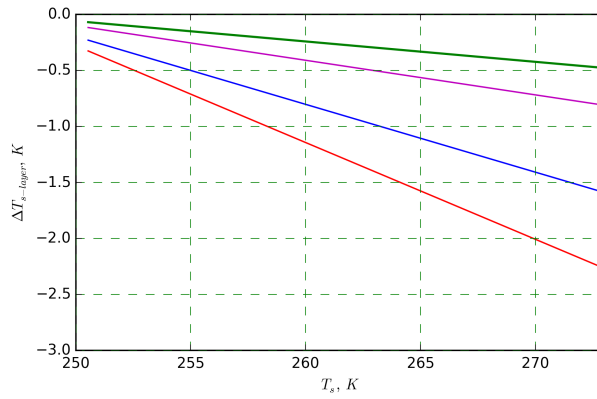
Figure B3. Temperature difference between the drop surface and internal drop layers calculated from the numerical simulation: drop center (red curve); layers number 5 (blue) and 8 (green) representing 20% and 60% of entire drop volume, respectively; and volume average temperature (magenta).
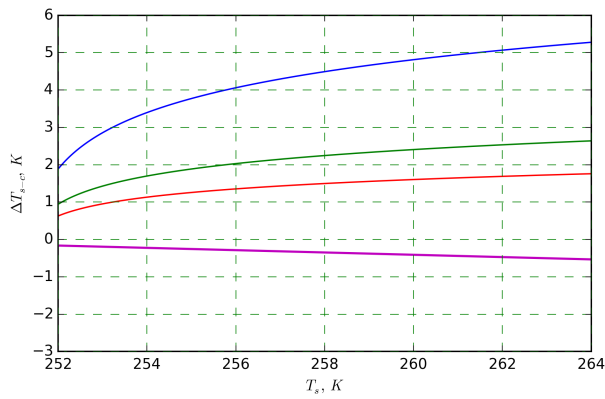
Figure B4. Temperature shift calculated for three different λ values (red: 0.8, green: 1.6., and blue: 2.4) in relation to temperature difference between drop surface and volume averaged drop temperature (magenta curve).

B5   Procedure chart for data evaluation
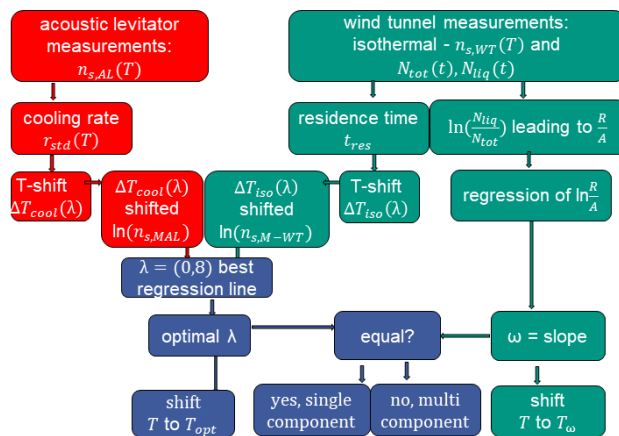
Figure B5. Flow chart of the procedure used to combine M-WT and M-AL measurement data for determining λ and ω and classifying the investigated materials as single or multiple-component. Red and green boxes are corresponding to M-Al and M-WT data, respectively.

Author contributions. MS wrote the paper with assistance from all co-authors contributing comments on results, discussion and conclusion; MS analysed the data, performed the numerical simulations, and carried out M-WT experiments on feldspar, FC, and MCC; MS and SKM conceived the M-AL and M-WT experiments; M. D. performed M-AL experiments on illite NX, kaolinite, and montmorillonite and evaluated the results; A. M. performed M-AL experiments on FC, and MCC, and evaluated the results; C.P.L. performed M-AL and M-WT experiments on feldspar and SDB01; O.E. performed M-AL and M-WT experiments on FC, MCC, illite NX, and feldspar.

Competing interests. The authors declare that they have no conflict of interest.

Acknowledgements. The authors acknowledge support from Deutsche Forschungsgemeinschaft (DFG) under contract SZ260/4-2 within Research Unit INUIT (FOR 1525). We also thank Prof. Holger Tost for his help in the statistical test methodology.

List of Symbols

The next list describes several symbols that will be later used within the body of the document

β freezing temperature shift for water vapor (Vali, 2014)

δN_{fr} number of droplets freezing within time interval δt

ΔT_{iso} temperature shift in isothermal experiments due to a relative change in residence time

$\Delta T_r, \Delta T_f$ absolute and normalized temperature shifts, respectively, in cooling experiments due to any change in cooling rate

δ Temperature difference between a drop and its environment in equilibrium (i.e., $\delta = T_\infty - T_e$))

λ Temperature gradient (K^{-1}) of the heterogeneous nucleation rate coefficient, J_s

ω Temperature gradient (K^{-1}) of the freezing rate

τ time constant of the temperature adaptation of a drop placed in cold/warm environment

A total particle surface area

c particle mass concentration in the sample solution

$f_i ce$ cumulative fraction of droplets frozen between $0\,^\circ\mathrm{C}$ and temperature T

J_s heterogeneous nucleation rate coefficient of a single component system

J_{hom} homogeneous nucleation rate coefficient

n_s ice nucleation active site density

n_{fr}, n_{liq} number of frozen and liquid droplets in a freezing experiment, respectively

N_{tot} total number of droplets in the population

$R(T)$ Freezing rate at a fixed temperature

765    $R(t,T)$ Rate of supercooled droplets freezing per unit time at a fixed temperature

r Cooling rate in the experiments

$s_\omega\, s_\lambda$ error weighted standard deviations of the residuals for ω and λ

SSA specific surface area of the particle

T Temperature

770   t measurement time

T_a Drop surface temperature

T_e Equilibrium temperature between ventilated evaporating droplet and its environment

T_∞ Air/environmental temperature

$t_{s,\omega}\, t_{s,\lambda}$ t-numbers corresponding to ω, and λ calculated for applying a two-sided Student t-test

775   t_{sig} t-number corresponding to a significance level of $99.9\,\%$ in a two-sided Student t-test

V_d aqueous suspension drop volume

References

Alpert, P. A. and Knopf, D. A.: Analysis of isothermal and cooling-rate-dependent immersion freezing by a unifying stochastic ice nucleation model, Atmospheric Chemistry and Physics, 16, 2083–2107, https://doi.org/10.5194/acp-16-2083-2016, https://acp.copernicus.org/
780   articles/16/2083/2016/, 2016.

Atkinson, J. D., Murray, B. J., Woodhouse, M. T., Whale, T. F., Baustian, K., Carslaw, K., Dobbie, S., O'Sullivan, D., and Malkin, T. L.: The importance of feldspar for ice nucleation by mineral dust in mixed-phase clouds, Nature, 498, 355 EP –, https://doi.org/10.1038/nature12278, 2013.

Barahona, D.: Bias-Free Estimation of Ice Nucleation Efficiencies, Geophysical Research Letters, 47, e2019GL086 033,
785   https://doi.org/https://doi.org/10.1029/2019GL086033,   https://agupubs.onlinelibrary.wiley.com/doi/abs/10.1029/2019GL086033,
        e2019GL086033 10.1029/2019GL086033, 2020.

Beard, K.: Terminal Velocity and Shape of Cloud and Precipitation Drops Aloft, Journal of the Atmospheric Sciences, 33, 851–864, http://dx.doi.org/10.1175%2F1520-0469%281976%29033%3C0851%3ATVASOC%3E2.0.CO%3B2, 1976.

Broadley, S. L., Murray, B. J., Herbert, R. J., Atkinson, J. D., Dobbie, S., Malkin, T. L., Condliffe, E., and Neve, L.: Immersion mode
790   heterogeneous ice nucleation by an illite rich powder representative of atmospheric mineral dust, Atmos. Chem. Phys., 12, 287–307, https://doi.org/10.5194/acp-12-287-2012, 2012.

Budke, C. and Koop, T.: BINARY: an optical freezing array for assessing temperature and time dependence of heterogeneous ice nucleation, Atmos. Meas. Tech., 8, 689–703, https://doi.org/10.5194/amt-8-689-2015, http://www.atmos-meas-tech.net/8/689/2015/, 2015.

Connolly, P. J., Möhler, O., Field, P. R., Saathoff, H., Burgess, R., Choularton, T., and Gallagher, M.: Studies of heterogeneous freez-
795   ing by three different desert dust samples, Atmos. Chem. Phys., 9, 2805–2824, https://doi.org/10.5194/acp-9-2805-2009, http://www.atmos-chem-phys.net/9/2805/2009/, 2009.

DeMott, P. J.: Quantitative descriptions of ice formation mechanisms of silver iodide-type aerosols, Atmospheric Research, 38, 63–99, https://doi.org/10.1016/0169-8095(94)00088-U, 1995.

DeMott, P. J., Möhler, O., Cziczo, D. J., Hiranuma, N., Petters, M. D., Petters, S. S., Belosi, F., Bingemer, H. G., Brooks, S. D., Budke, C.,
800   Burkert-Kohn, M., Collier, K. N., Danielczok, A., Eppers, O., Felgitsch, L., Garimella, S., Grothe, H., Herenz, P., Hill, T. C. J., Höhler, K., Kanji, Z. A., Kiselev, A., Koop, T., Kristensen, T. B., Krüger, K., Kulkarni, G., Levin, E. J. T., Murray, B. J., Nicosia, A., O'Sullivan, D., Peckhaus, A., Polen, M. J., Price, H. C., Reicher, N., Rothenberg, D. A., Rudich, Y., Santachiara, G., Schiebel, T., Schrod, J., Seifried, T. M., Stratmann, F., Sullivan, R. C., Suski, K. J., Szakáll, M., Taylor, H. P., Ullrich, R., Vergara-Temprado, J., Wagner, R., Whale, T. F., Weber, D., Welti, A., Wilson, T. W., Wolf, M. J., and Zenker, J.: The Fifth International Workshop on Ice Nucleation phase 2 (FIN-02):
805   Laboratory intercomparison of ice nucleation measurements, Atmos. Meas. Tech., 11, 6231–6257, https://doi.org/10.5194/amt-11-6231-2018, 2018.

Diehl, K. and Grützun, V.: Model simulations with COSMO-SPECS: Impact of heterogeneous freezing modes and ice nucleating particle types on ice formation and precipitation in a deep convective cloud, Atmospheric Chemistry and Physics, 18, 3619–3639, https://doi.org/10.5194/acp-18-3619-2018, https://www.atmos-chem-phys.net/18/3619/2018/, 2018.

810   Diehl, K., Mitra, S. K., Szakáll, M., Blohn, N., Borrmann, S., and Pruppacher, H. R.: The Mainz Vertical Wind Tunnel Facility-A Review of 25 Years of Laboratory Eexperiments on Cloud Physics And Chemistry: in: Wind Tunnels: Aerodynamics, Models and Experiments, Nova Science Publishers, Inc., Hauppage, 2011.

Diehl, K., Debertshäuser, M., Eppers, O., Schmithüsen, H., Mitra, S. K., and Borrmann, S.: Particle surface area dependence of mineral dust in immersion freezing mode: investigations with freely suspended drops in an acoustic levitator and a vertical wind tunnel, Atmos. Chem. Phys., 14, 12 343–12 355, https://doi.org/10.5194/acp-14-12343-2014, http://www.atmos-chem-phys.net/14/12343/2014/, 2014.

Ettner, M., Mitra, S. K., and Borrmann, S.: Heterogeneous freezing of single sulfuric acid solution droplets: Laboratory experiments utilizing an acoustic levitator, Atmospheric Chemistry and Physics, 4, 1925–1932, https://doi.org/10.5194/acp-4-1925-2004, https://www.atmos-chem-phys.net/4/1925/2004/, 2004.

Hader, J. D., Wright, T. P., and Petters, M. D.: Contribution of pollen to atmospheric ice nuclei concentrations, Atmospheric Chemistry and Physics, 14, 5433–5449, https://doi.org/10.5194/acp-14-5433-2014, https://www.atmos-chem-phys.net/14/5433/2014/, 2014.

Harrison, A. D., Whale, T. F., Rutledge, R., Lamb, S., Tarn, M. D., Porter, G. C. E., Adams, M. P., McQuaid, J. B., Morris, G. J., and Murray, B. J.: An instrument for quantifying heterogeneous ice nucleation in multiwell plates using infrared emissions to detect freezing, Atmos. Meas. Tech., 11, 5629–5641, https://doi.org/10.5194/amt-11-5629-2018, 2018.

Hartmann, S., Wex, H., Clauss, T., Augustin-Bauditz, S., Niedermeier, D., Rösch, M., and Stratmann, F.: Immersion Freezing of Kaolinite: Scaling with Particle Surface Area, Journal of the Atmospheric Sciences, 73, 263–278, https://doi.org/10.1175/JAS-D-15-0057.1, 2016.

Herbert, R. J., Murray, B. J., Whale, T. F., Dobbie, S. J., and Atkinson, J. D.: Representing time-dependent freezing behaviour in immersion mode ice nucleation, Atmos. Chem. Phys., 14, 8501–8520, https://doi.org/10.5194/acp-14-8501-2014, 2014.

Hindmarsh, J., Russell, A., and Chen, X.: Experimental and numerical analysis of the temperature transition of a suspended freezing water droplet, International Journal of Heat and Mass Transfer, 46, 1199–1213, https://doi.org/10.1016/S0017-9310(02)00399-X, 2003.

Hiranuma, N., Augustin-Bauditz, S., Bingemer, H., Budke, C., Curtius, J., Danielczok, A., Diehl, K., Dreischmeier, K., Ebert, M., Frank, F., Hoffmann, N., Kandler, K., Kiselev, A., Koop, T., Leisner, T., Möhler, O., Nillius, B., Peckhaus, A., Rose, D., Weinbruch, S., Wex, H., Boose, Y., DeMott, P. J., Hader, J. D., Hill, T. C. J., Kanji, Z. A., Kulkarni, G., Levin, E. J. T., McCluskey, C. S., Murakami, M., Murray, B. J., Niedermeier, D., Petters, M. D., O'Sullivan, D., Saito, A., Schill, G. P., Tajiri, T., Tolbert, M. A., Welti, A., Whale, T. F., Wright, T. P., and Yamashita, K.: A comprehensive laboratory study on the immersion freezing behavior of illite NX particles: A comparison of 17 ice nucleation measurement techniques, Atmospheric Chemistry and Physics, 15, 2489–2518, https://doi.org/10.5194/acp-15-2489-2015, https://www.atmos-chem-phys.net/15/2489/2015/, 2015.

Hiranuma, N., Adachi, K., Bell, D. M., Belosi, F., Beydoun, H., Bhaduri, B., Bingemer, H., Budke, C., Clemen, H.-C., Conen, F., Cory, K. M., Curtius, J., DeMott, P. J., Eppers, O., Grawe, S., Hartmann, S., Hoffmann, N., Höhler, K., Jantsch, E., Kiselev, A., Koop, T., Kulkarni, G., Mayer, A., Murakami, M., Murray, B. J., Nicosia, A., Petters, M. D., Piazza, M., Polen, M., Reicher, N., Rudich, Y., Saito, A., Santachiara, G., Schiebel, T., Schill, G. P., Schneider, J., Segev, L., Stopelli, E., Sullivan, R. C., Suski, K., Szakáll, M., Tajiri, T., Taylor, H., Tobo, Y., Ullrich, R., Weber, D., Wex, H., Whale, T. F., Whiteside, C. L., Yamashita, K., Zelenyuk, A., and Möhler, O.: A comprehensive characterization of ice nucleation by three different types of cellulose particles immersed in water, Atmospheric Chemistry and Physics, 19, 4823–4849, https://doi.org/10.5194/acp-19-4823-2019, https://www.atmos-chem-phys.net/19/4823/2019/, 2019.

Hoose, C. and Möhler, O.: Heterogeneous ice nucleation on atmospheric aerosols: A review of results from laboratory experiments, Atmospheric Chemistry and Physics, 12, 9817–9854, https://doi.org/10.5194/acp-12-9817-2012, https://www.atmos-chem-phys.net/12/9817/2012/, 2012.

Ishizaka, S., Wada, T., and Kitamura, N.: In situ observations of freezing processes of single micrometer-sized aqueous ammonium sulfate droplets in air, Chemical Physics Letters, 506, 117–121, https://doi.org/10.1016/j.cplett.2011.02.058, 2011.

Knopf, D. A., Alpert, P. A., Zipori, A., Reicher, N., and Rudich, Y.: Stochastic nucleation processes and substrate abundance explain time-dependent freezing in supercooled droplets, npj Climate and Atmospheric Science, 3, https://doi.org/10.1038/s41612-020-0106-4, 2020.

Lierke, E. G.: Vergleichende Betrachtungen zur berührungslosen Positionierung von Einzeltropfen in aerodynamischen, akustischen und elektrischen Kraftfeldern, Forschung im Ingenieurwesen, 61, 201–216, https://doi.org/10.1007/BF02609485, 1995.

Murray, B. J., Broadley, S. L., Wilson, T. W., Atkinson, J. D., and Wills, R. H.: Heterogeneous freezing of water droplets containing kaolinite particles, Atmos. Chem. Phys., 11, 4191–4207, https://doi.org/10.5194/acp-11-4191-2011, http://www.atmos-chem-phys.net/11/4191/2011/, 2011.

Murray, B. J., O'Sullivan, D., Atkinson, J. D., and Webb, M. E.: Ice nucleation by particles immersed in supercooled cloud droplets, Chemical Society Reviews, 41, 6519–6554, https://doi.org/10.1039/C2CS35200A, 2012.

Niedermeier, D., Hartmann, S., Shaw, R. A., Covert, D., Mentel, T. F., Schneider, J., Poulain, L., Reitz, P., Spindler, C., Clauss, T., Kiselev, A., Hallbauer, E., Wex, H., Mildenberger, K., and Stratmann, F.: Heterogeneous freezing of droplets with immersed mineral dust particles – measurements and parameterization, Atmospheric Chemistry and Physics, 10, 3601–3614, https://doi.org/10.5194/acp-10-3601-2010, https://acp.copernicus.org/articles/10/3601/2010/, 2010.

Peckhaus, A., Kiselev, A., Hiron, T., Ebert, M., and Leisner, T.: A comparative study of K-rich and Na/Ca-rich feldspar ice-nucleating particles in a nanoliter droplet freezing assay, Atmospheric Chemistry and Physics, 16, 11 477–11 496, https://doi.org/10.5194/acp-16-11477-2016, https://www.atmos-chem-phys.net/16/11477/2016/, 2016.

Pruppacher, H. R. and Klett, J. D.: Microphysics of clouds and precipitation, Springer, 2010.

Reicher, N., Segev, L., and Rudich, Y.: The WeIzmann Supercooled Droplets Observation on a Microarray (WISDOM) and application for ambient dust, Atmos. Meas. Tech., 11, 233–248, https://doi.org/10.5194/amt-11-233-2018, 2018.

Rigg, Y. J., Alpert, P. A., and Knopf, D. A.: Immersion freezing of water and aqueous ammonium sulfate droplets initiated by humic-like substances as a function of water activity, Atmospheric Chemistry and Physics, 13, 6603–6622, https://doi.org/10.5194/acp-13-6603-2013, https://acp.copernicus.org/articles/13/6603/2013/, 2013.

Rzesanke, D., Nadolny, J., Duft, D., Müller, R., Kiselev, A., and Leisner, T.: On the role of surface charges for homogeneous freezing of supercooled water microdroplets, Physical Chemistry Chemical Physics, 14, 9359–9363, https://doi.org/10.1039/C2CP23653B, 2012.

Schrod, J., Danielczok, A., Weber, D., Ebert, M., Thomson, E. S., and Bingemer, H. G.: Re-evaluating the Frankfurt isothermal static diffusion chamber for ice nucleation, Atmos. Meas. Tech., 9, 1313–1324, https://doi.org/10.5194/amt-9-1313-2016, 2016.

Szakáll, M., Mitra, S. K., Diehl, K., and Borrmann, S.: Shapes and oscillations of falling raindrops – A review, Atmospheric Research, 97, 416–425, http://www.sciencedirect.com/science/article/pii/S0169809510000736, 2010.

Ullrich, R., Hoose, C., Möhler, O., Niemand, M., Wagner, R., Höhler, K., Hiranuma, N., Saathoff, H., and Leisner, T.: A New Ice Nucleation Active Site Parameterization for Desert Dust and Soot, Journal of the Atmospheric Sciences, 74, 699–717, https://doi.org/10.1175/JAS-D-16-0074.1, https://doi.org/10.1175/JAS-D-16-0074.1, 2017.

Vali, G.: Freezing Rate Due to Heterogeneous Nucleation, J. Atmos. Sci., 51, 1843–1856, https://doi.org/10.1175/1520-0469(1994)051<1843:FRDTHN>2.0.CO;2, 1994.

Vali, G.: Interpretation of freezing nucleation experiments: Singular and stochastic; sites and surfaces, Atmos. Chem. Phys., 14, 5271–5294, https://doi.org/10.5194/acp-14-5271-2014, 2014.

Vali, G. and Stansbury, E. J.: Time-dependent characteristics of heterogeneous nucleation of ice, Canadian Journal of Physics, 44, 477–502, https://doi.org/10.1139/p66-044, 1966.

Vali, G., DeMott, P. J., Möhler, O., and Whale, T. F.: Technical Note: A proposal for ice nucleation terminology, Atmos. Chem. Phys., 15, 10 263–10 270, https://doi.org/10.5194/acp-15-10263-2015, 2015.

von Blohn, N., Mitra, S. K., Diehl, K., and Borrmann, S.: The ice nucleating ability of pollen. Part III: New labora­tory studies in immersion and contact freezing modes including more pollen types, Atmospheric Research, 78, 182–189, https://doi.org/10.1016/j.atmosres.2005.03.008, 2005.

Welti, A., Lüönd, F., Kanji, Z. A., Stetzer, O., and Lohmann, U.: Time dependence of immersion freezing: An experimental study on size selected kaolinite particles, Atmospheric Chemistry and Physics, 12, 9893–9907, https://doi.org/10.5194/acp-12-9893-2012, https://www.atmos-chem-phys.net/12/9893/2012/, 2012.

Whale, T. F., Murray, B. J., O'Sullivan, D., Wilson, T. W., Umo, N. S., Baustian, K. J., Atkinson, J. D., Workneh, D. A., and Morris, G. J.: A technique for quantifying heterogeneous ice nucleation in microlitre supercooled water droplets, Atmos. Meas. Tech., 8, 2437–2447, https://doi.org/10.5194/amt-8-2437-2015, http://www.atmos-meas-tech.net/8/2437/2015/, 2015.

Wright, T. P. and Petters, M. D.: The role of time in heterogeneous freezing nucleation, Journal of Geophysical Research: Atmospheres, 118, 3731–3743, https://doi.org/10.1002/jgrd.50365, https://agupubs.onlinelibrary.wiley.com/doi/abs/10.1002/jgrd.50365, 2013.